~~Two different phytoplankton~~Phytoplankton blooming mechanisms over the East China Sea during El- Niño decaying summers

Dong-Geon Lee[1,2], Ji-Hoon Oh[2], Jonghun Kam[1,] Jong-Seong Kug*[2]

[1]Division of Environmental Science and Engineering, Pohang University of Science and Technology (POSTECH), Pohang, South Korea

[2]School of Earth and Environmental Sciences, Seoul National University, Seoul, South Korea

Correspondence to: Jong-Seong Kug (jskug@snu.ac.kr)

Abstract. During an El Niño-decaying summer, the East China Sea (ECS) has experienced anomalous phytoplankton blooming, but the understanding of associated generating mechanisms remains limited. Here, we analyzed observational (25 years) and long-term simulation data (1,000 years) to investigate the underlying mechanisms for the anomalous phytoplankton blooming in ECS. Results highlight ~~two~~three mechanisms associated with enhanced phytoplankton blooming in ECS during El Niño-decaying summers: inland runoff-~~driven~~, nutrient inputs from the Taiwan Strait (TS), and oceanic sub-surface upwelling-driven blooming mechanisms. Firstly, increased river discharge from the Yangtze River (YR) induces phytoplankton blooms. Secondly, enhanced nutrient inputs through TS promote phytoplankton growth. Additionally, wind-driven Ekman upwelling in ECS provides nutrients for phytoplankton growth from the sub-surface to the surface water layer. ~~Rossby wave propagations from~~These three mechanisms are all linked to the Western North Pacific Anti-Cyclone (WNPAC~~) cause~~), suggesting the WNPAC can be a ~~distinctive cyclonic atmospheric circulation over~~key precursor to predict ECS ~~that induces Ekman upwelling. The climate~~blooming. Climate model ~~simulation supports~~simulations support these ~~two~~complex mechanisms, and thus our results suggest that ~~both~~all mechanisms can contribute to the phytoplankton bloom concurrently.

1. Introduction

Numerous rivers, including ~~The~~the Yangtze River (YR), run into the East China Sea (ECS). YR is the longest river in Eurasia, contributing to a shallow continental shelf with high marine primary productivity ~~(Liu et al., 2010, 2003; Tong et al., 2015; Zhai et al., 2023; Zhang, 1996; Zhao and Guo, 2011).~~(Zhai et al., 2023; Zhang, 1996; Liu et al., 2003; Zhao and Guo, 2011; Tong et al., 2015; Liu et al., 2010). Particularly, the Yellow Sea (YS) and ECS, which belong to the East Asian Marginal Seas (EAMS), are known for being among the most productive marine environments globally. Nutrients for phytoplankton growth are ample from the intrusion of nutrient-rich Kuroshio intermediate water ~~(Chen, 1996; Chen et al., 1995; Zhang et al., 2007)~~through the Taiwan Strait (TS; Chen, 1996; Chen et al., 1995; Zhang et al., 2007), atmospheric deposition (Kim et al., 2011; Zhang et al., 2010), and primarily riverine input from the YR ~~(Huang et al., 2019; Wang et al., 2003).~~(Wang et al., 2003; Huang et al., 2019).

Marine phytoplankton plays a role in the marine trophic chain (Danielsdottir et al., 2007), ocean carbon, and biogeochemical cycles ~~(Behrenfeld et al., 2006; Field et al., 1998).~~(Field et al., 1998; Behrenfeld et al., 2006). Chlorophyll-a (Chl-a) concentration is widely used as a proxy for phytoplankton biomass and it has strength for handiness to measure from satellite (Henson et al., 2010). The ECS region is surrounded by highly populated and developed nations with hundreds of_ millions of people, which can have a profound impact on fisheries and marine ecosystems. Therefore, understanding the spatio-temporal variability of phytoplankton in the ECS region ~~associated with changes in river discharge~~ has great socio-economic importance, particularly in coastal communities.

ENSO plays a key role as a climate regulator for East Asia through its teleconnection. The Western North Pacific ~~Anti Cyclone~~AntiCyclone (WNPAC) regulates the East Asian climate during ENSO events from the developing to decaying ~~phase~~phases ~~(Kim and Kug, 2018; Li et al., 2017; Son et al., 2014; Wang et al., 2000).~~(Wang et al., 2000; Son et al., 2014; Li et al., 2017; Kim and Kug, 2018). ENSO-induced changes in the atmospheric and oceanic circulation alter physical properties in the ECS region, which can also affect the marine ecosystems of the ECS region ~~(Racault et al., 2017). During a decaying El~~(He et al., 2013; Xu et al., 2022; Wu et al., 2023). During a decaying El Niño summer season, anomalous WNPAC transports warm and moist air from lower latitudes to East Asia, which increases regional precipitation ~~(Kwon et al., 2005; Li et al., 2021) and thus river discharge, carrying abundant nutrients into the YECS~~(Li et al., 2021; Kwon et al., 2005) and thus river discharge, carrying abundant nutrients into the Yellow and East China Seas (YECS) region ~~(Beardsley et al., 1985; Shi and Wang, 2012).~~(Shi and Wang, 2012; Beardsley et al., 1985; He et al., 2013; Wu et al., 2023). This augmented river discharge impacts the coastal ecosystems of eastern China and the western part of the Korean peninsula, potentially triggering anomalous phytoplankton blooming ~~(He et al., 2013; Park et al., 2015; Yamaguchi et al., 2012).~~(He et al., 2013; Yamaguchi et al., 2012; Park et al., 2015). In addition, during this period, anomalous southwesterly winds drive more nutrient-rich water from the South China Sea (SCS) into the ECS through the TS (Zhang et al., 2015; Huang et al., 2015). The recent increasing trend in surface chlorophyll-a in the ECS is correlated with nutrient concentrations without an increase in river discharge (He et al., 2013). In addition, increased river discharge can cause anomalous phytoplankton blooming after strong El Niño cases (Wu et al.,

61   2023). These results suggest that ~~there~~various processes can ~~be another process to~~ induce ~~the~~ enhanced
62   phytoplankton blooming during El Niño decaying summer.

63   The WNPAC generated during the El Niño period not only increases riverine flows and nutrient
64   transport from TS but also accompanies anomalous cyclonic circulation over the EAMS region by the atmospheric
65   Rossby wave propagation. This induces Ekman upwelling (EKU) in the ECS region, transporting nutrients from
66   the oceanic sub-surface to the surface layer, and fostering anomalous phytoplankton blooming. Together with
67   nutrient inputs via river discharge and the TS, this upwelling-driven mechanism could further amplify productivity
68   during these periods. An improved understanding of the ~~additional mechanism~~various complex mechanisms in
69   conjunction ~~with the existing one,~~, it will allow us to more accurately estimate the magnitude of phytoplankton
70   blooms in the ECS region during post-~~-~~El Niño summers. This could have implications for marine resource
71   management and fisheries in many neighboring countries.

72   ~~Here, we propose another mechanism other than nutrient fluxes from the enhanced inland river~~
73   ~~discharge. This study aims to~~ Here, we aim to comprehensively understand the variability of phytoplankton
74   concentrations in the ECS region during the El Niño-decaying summers. We investigate ~~both~~all of the
75   phytoplankton blooming mechanisms: inland ~~runoff~~riverine inflow and buoyancy upwelling by river discharge,
76   nutrient inputs from the TS, and wind-driven ~~and~~ oceanic sub-surface upwelling ~~driven blooming~~ and quantify
77   the relative contributions of these three mechanisms ~~during El Niño decaying summers~~. The climate model long-
78   term simulation and observational data support these findings, highlighting the concurrent roles of both
79   mechanisms in enhancing phytoplankton blooming.

80 **2. Data and Methods**

81 **2.1. Reanalysis & Observation data**

82   We used the ocean colour satellite data from the European Space Agency Climate Change Initiative

83 Version (ESA-CCI) for chlorophyll-a data, serving as a proxy for phytoplankton biomass, covering 25-year

84 periods from 1998 to 2022 (Sathyendranath et al., 2019). El Niño events were identified using Extended

85 Reconstructed Sea Surface Temperature version 5 (ERSSTv5; Huang et al., 2017) Sea Surface Temperature (SST)

86 data from National Oceanic and Atmospheric Administration (NOAA), with anomalies greater than 1 standard

87 deviation during the winter season (December – January – February; DJF) index in the Nino3.4 (5°S-5°N / 170°

88 W-120°W) region. Furthermore, to examine atmospheric circulation such as wind, precipitation, and geopotential

89 height (GPH) changes, we analyzed the re-analysis data from the National Centers for Environmental Prediction

90 reanalysis version 2 / the National Center for Atmospheric Research (NCEP2 / NCAR; Kanamitsu et al., 2002).

91 Lastly, wind stress (τ) and wind stress curl (Curl$_{(\tau)}$; Kessler, 2006) are calculated followed as Eqs. (1)-(2) with

92 typical value for drag coefficient (C_D = 0.0015~~; Trenberth et al., 1990; Wyrtki and Meyers, 1976)~~; Trenberth et

93 al., 1990; Wyrtki and Meyers, 1976) and sea level air density (ρ_{air} = 1.225 kg m^{-3}; Cavcar, 2000) with the

94 square of zonal & meridional wind speed (V^2) from NCEP2 re-analysis data. In addition, we used Simple Ocean

95 Data Assimilation (SODA), version 3 from 1980 to 2020 to investigate the ocean currents (Carton et al., 2018).

96 We used nutrients (Phosphate; PO$_4$) data from Copernicus Marine Environment Monitoring Service (CMEMS)

97 Biogeochemical hindcast (10.48670/moi-00019) at monthly timesteps from 1998 to 2023. We calculated

98 meridional PO$_4$ transport by multiplying the PO$_4$ concentration and meridional ocean current velocity, which was

99 vertically integrated up to 50 m as Eq. (3) for the period from 1998 to 2020, when both data are available.

100     $-\tau = \rho_{air} C_D V^2$

101   (1)

102     $\text{Curl}_{(\tau)} = \frac{\partial \tau_y}{\partial x} - \frac{\partial \tau_x}{\partial y}$

103   (2)

104     $\int_{10m}^{50m} PO_4 \cdot v \ current \ velocity \ dz$ (3)

105

106 **2.2. Model data**

107   We used the present climate-based (1990-year atmospheric CO_2 concentration level; 353 parts per

108 million (ppm)) long-term ~~integrated~~(1,000 years) simulations of the Geophysical Fluid Dynamic Laboratory

109 (GFDL) - CM2.1 Earth System Model (ESM) fully coupled with the marine ecosystem model TOPAZv2 (Tracers

110 of Ocean Phytoplankton with Allometric Zooplankton Version 2; Dunne et al., 2013). The model incorporates

111 various external nutrient inputs such as atmospheric deposition, river nitrogen (N) input, and river inputs of

112 dissolved carbon, alkalinity, and lithogenic material; however not includes river phosphorus (P) inputs (Dunne et

113 al., 2013). The growth rate of phytoplankton is computed using a function of chlorophyll to carbon ratio and

114 limited by various factors in TOPAZ (Dunne et al., 2010). Nutrient limitation terms are determined by minimum

115 limitation values among macronutrients & micronutrients (Fe, PO_4, $Si(OH)_4$, $NO_3 + NH_4$).

116   Surface values in the model data were averaged to 30-meter depths, with spatial grid and temporal scale

117 set at 1° x 1° grid and monthly mean data, respectively. All anomalies are calculated by removing the seasonal

118 cycles and the linear trend. El Niño events were defined in the same ~~methodology~~way as in the observation data.

119 Statistical significance was calculated using the non-parametric bootstrap method, with 10,000 random samples

120 replacing as many numbers of El Niño cases in observation and model results, respectively.

121

3. Results

3.1. Runoff & TS-transport-driven blooming ~~mechanism~~mechanisms - Insight from Observations

~~Figures 1a b display the composite maps illustrating the spatial distribution of surface chlorophyll-a anomalies (SCHL) and precipitation anomalies during the El Niño decaying summer season (June-July-August; JJA). The pronounced anomalous SCHL blooming is observed from the Yangtze River Estuary (YRE) to the southern part of the Korean Peninsular. It has consistent patterns with the dispersal of strong river discharge from the YR (Park et al., 2015; Yamaguchi et al., 2012). In addition to the estuary of the YR region, there are also broad weak diagonal patterns of positive signal from northeastern Taiwan to the Korean Strait. This is in agreement with the relationship between Yangtze River Discharge (YRD) and SCHL in Yamaguchi et al, which has a lagged correlation from June to August and extends over a wide region from Jeju Island to the Korean Strait.~~
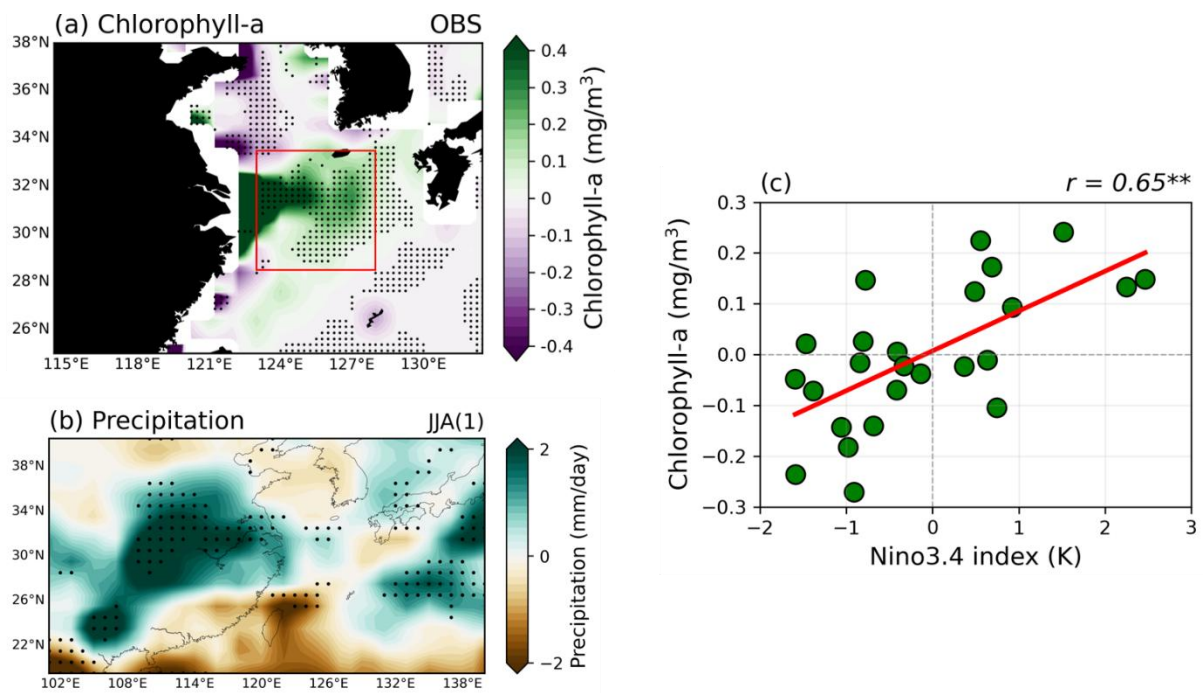
Figures 1a displays the composite maps illustrating the spatial distribution of surface chlorophyll-a anomalies (SCHL) during the El Niño decaying summer season (June-July-August; JJA). The pronounced anomalous SCHL blooming is observed from the Yangtze River Estuary (YRE) to the southern part of the Korean Peninsula. It has consistent patterns with the dispersal of strong river discharge from the YR (Yamaguchi et al., 2012; Park et al., 2015). In addition to the estuary of the YR region, broad, weak diagonal patterns of positive signals are also observed extending from northeastern Taiwan to the Korean Strait. This is in agreement with the relationship between Yangtze River Discharge (YRD) and SCHL in Yamaguchi et al. (2012) which has a lagged correlation from June to August and extends over a wide region from Jeju Island to the Korean Strait.
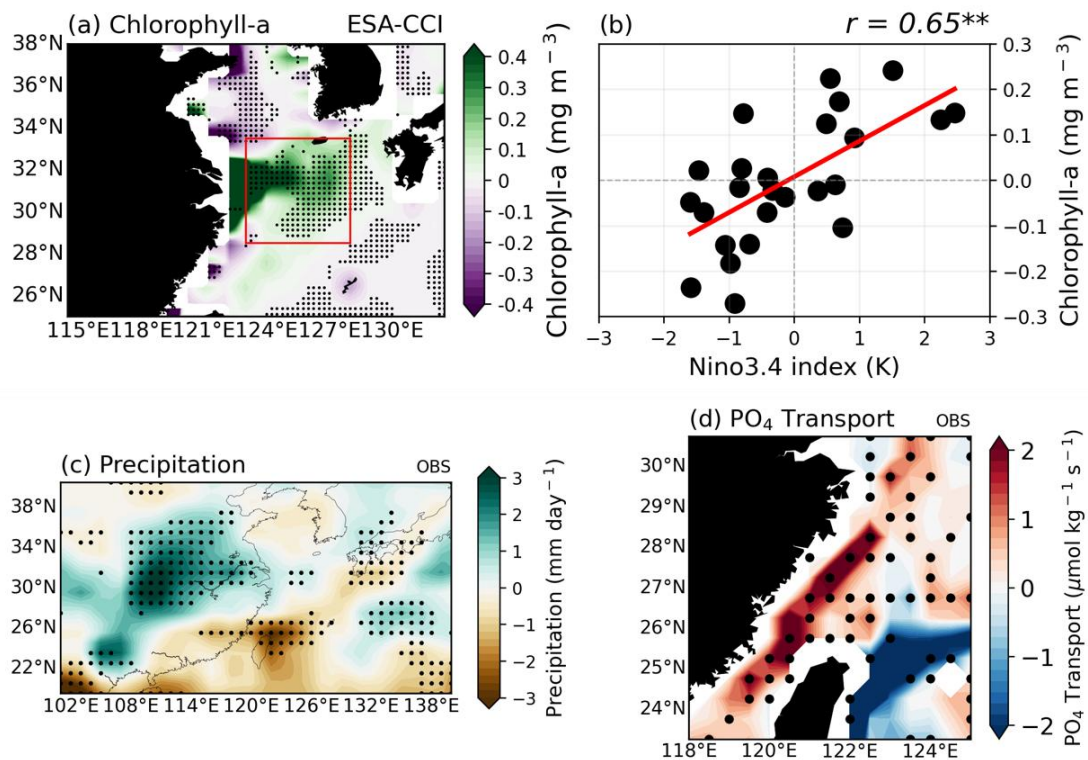
Figure 1. Composite maps exhibiting the 3-month average of **(a)** surface Chlorophyll-a (SCHL) anomalies, and (b) precipitation anomalies for using satellite data during the El Niño decaying summer season (June-July-August; JJA) of all El Niño cases, using re-analysis and satellite data. (c. **(b)** The relationship between the Niño3.4-DJF index which indicates the strength of El Niño mature phase and area-averaged SCHL anomalies over the research target area during the El Niño decaying summer season (Red box in Fig. 1a; 28.5°N-33.5°N / 122.5123°E-128.5°E).°E). **(c)** Precipitation anomalies for El Niño decaying summer season (June-July-August; JJA) of all El Niño cases, using re-analysis and satellite data. **(d)** Meridional PO₄ transport anomalies through the Taiwan Strait (TS) for El Niño decaying summer season of all El Niño cases in reanalysis. All the black dots indicate where the responses are significant at the 9590% confidence level by using the bootstrap method. ** marks indicate statistically significant correlation at the 99% confidence level.

ThisDuring the El Niño decaying summers (JJA(1)), the lagged correlation between the Nino3.4 D(0)JF(1) index and the SCHL anomalies in the ECS region (28.5°N-33.5°N, 123°E-128°E; target region indicated as red box in Fig. 1a) indicate significant positive relationship (r = 0.65**) at the 99% confidence level (Figure 1b). The anomalous phytoplankton bloomblooms during the boreal summer season of the summers following El Niño events has been explainedcan be attributed to increased riverine discharge from the YR, driven by enhanced precipitation., and the substantial nutrient supply through the TS from the South China Sea (SCS). In the El NinoNiño years, the intensification of southwesterly winds by the Western North Pacific (WNP) high-pressureanticyclone flow brings in warm and humid air from lower latitudes. This, in turn, leads to anomalous rainfall in the East Asian region (Figure 1b1c). Given the strong association between the variability of the YRD and precipitation, it is reasonable to anticipate that an increase in riverine input corresponds to increased precipitation (Park et al., 2015). The lagged correlation between the Nino3.4 D(0)JF(1) index and the SCHL

164 anomalies in the ECS region (28.5°N 33.5°N, 123°E 128°E; target region indicated as red box in Fig. 1a) during

165 El Niño decaying summers (JJA(1)) indicate significant positive relationship (r = 0.65**) at the 99% confidence

166 level (Figure 1c). In addition to the direct riverine nutrient input, enhanced river discharge can facilitate nutrients

167 to the ECS region through buoyancy upwelling (Chen, 2008; Chen et al., 2003; Chen, 2000; Hill, 1998). When

168 the out-flowing river plume becomes more substantial than the incoming river discharge, subsurface waters are

169 readily upwelled to preserve the water balance. Consequently, the nutrient-rich Kuroshio subsurface waters ascend

170 along the ECS shelf edge, providing essential nutrients. This buoyancy-driven upwelling occurs independently of

171 wind conditions, driven primarily by the physical properties of the subsurface waters in response to the intensified

172 river outflow.

173 Additionally, the WNP anticyclonic circulation and its curl intensify the sea level gradient of the

174 northwestern-southeastern regions over the SCS and thus amplify water transport through the TS, delivering

175 nutrient-rich SCS water into the ECS region during El Niño decaying summers (Figure 1d; Huang et al., 2015;

176 Zhang et al., 2015; Chen et al., 2015). The influx of nutrient-rich waters, particularly PO_4, further facilitates marine

177 phytoplankton in the ECS region.

178 To comprehensively understand the mechanisms ofdriving phytoplankton blooms overin the ECS

179 during the summer season afterfollowing the ENSO mature phase, we first re-assessed two major processes

180 suggested by several previous studies—the runoff-driven blooming mechanism, commonly well-known from

181 several previous studies. The and the TS-transport-driven blooming mechanism—as few studies have directly

182 compared them in the context of ECS phytoplankton blooms. In the runoff-driven mechanism, robust positive

183 signal in the precipitation anomalies is centered in the southeastern part of China, (where the YR flows. The)

184 lead to intensified precipitation,rainfall and consequently, triggers an increase in river discharge, leading. This

185 enhanced river discharge delivers additional nutrients to the ECS, not only through direct river inflow but also via

186 the entrainment of subsurface waters by buoyancy upwelling induced by the out-flowing river plume (Runoff-

187 driven mechanism). The TS-transport-driven mechanism is marked by positive meridional PO_4 transport signals,

188 indicating substantial nutrient flux into the ECS through the TS from the SCS during El Niño decaying summers.

189 This enhanced nutrient supply can significantly contribute to anomalous surface chlorophyll (SCHL blooming

190 broadly over the YECS (Runoff-driven blooming) blooms in the ECS, highlighting the critical role of TS inflow

191 in influencing phytoplankton growth. (TS-Transport-driven mechanism).

192

3.2. Runoff & TS-transport-driven blooming mechanismmechanisms - Insight from Model

194 We further analyzed a long-term simulation using the GFDL-CM2.1 ESM with a fully coupled

195 biogeochemical model to understand blooming mechanisms as well as the well-known runoff-driven blooming

196 mechanism. Notably, the GFDL-CM2.1 ESM does not simulate inputs of P from riverine inflowsvarious

197 phytoplankton blooming mechanisms. In our target area, the ECS region, climatologically, there is a strong influx

198 of riverine runoff from the YR, which contains excesscarries elevated Nitrate (N) concentrations (Kim et al., 2011;

199 Moon et al., 2021; Wang et al., 2003). Under these marine environmental ~~characteristics~~conditions, P is relatively

200 constrained, and phytoplankton growth is primarily controlled by changes in P concentrations. ~~In~~Although the

201 ~~oceans where~~GFDL-CM2.1 ESM does not simulate P ~~is the dominant factor regulating phytoplankton growth,~~

202 ~~especially in the target region, the deficiency of P~~ inputs from riverine ~~inputs in the models may underestimate~~

203 ~~phytoplankton variability. However, it affords~~inflows, it does account for P supply through the dynamic ascent of

204 subsurface waters driven by buoyancy upwelling resulting from intensified river discharge. Therefore, beyond

205 analyses based on observational and reanalysis data, long-term model simulations enable us ~~the advantage of~~

206 ~~exploring~~ to comprehensively understand the phytoplankton blooming mechanisms ~~from another perspective, not~~

207 ~~just a runoff-driven mechanism centered on the YRE region.~~ in the ECS during the following summers of El Niño

208 events.

209 Prior to delving into further analyses, we verified ~~that~~whether GFDL-CM2.1 ESM adequately simulates

210 the nutrient limitation in the target region (26.5°N-32.5°N, 122.5°E-128.5°E; target region in the model), with

211 strong P limitation observed in the YRE region and stronger N limitation appearing getting farther out (Figure 2).

212 We confirmed the nutrient limitation by separating the target region into the YRE and the extended YRE region

213 (red & blue box in Figs. 2e-f). In Figs. 2a-b, there is a relatively weak positive correlation ($r = 0.25$**) between

214 surface NO_3 and SCHL anomalies in the YRE region, while a higher significant positive correlation ($r = 0.72$**)

215 in the extended YRE region, indicating that N limitation begins to prevail. On the other hand, Figures 2c-d show

216 a significantly strong positive correlation ($r = 0.88$**) between surface PO_4 and SCHL anomalies in the YRE

217 region and no correlation ($r = -0.03$) over the extended YRE region. In particular, the partial correlation between

218 the surface PO_4 and SCHL anomalies after removing the effect of NO_3 in the YRE region is almost unchanged at

219 0.86**, while the opposite effect is even lower at 0.1**. The spatial distribution of partial correlations shows that

220 the effect of surface NO_3 on SCHL anomalies after removing the effect of surface PO_4 is stronger in the extended

221 YRE region. On the other hand, the effect of surface PO_4 on SCHL anomalies after removing the influence of

222 surface NO_3 is very strong not only in the YRE region but also over the YECS and Bohai Sea (Figures 2e-f). These

223 support the dominant P limitation in the YRE region, implying that the strong P limitation in the YRE region is

224 applied as well as the observations. These findings indicate the GFDL-CM2.1 ESM's ability to simulate the

225 relationship between phytoplankton growth and nutrients in the ECS region.

226
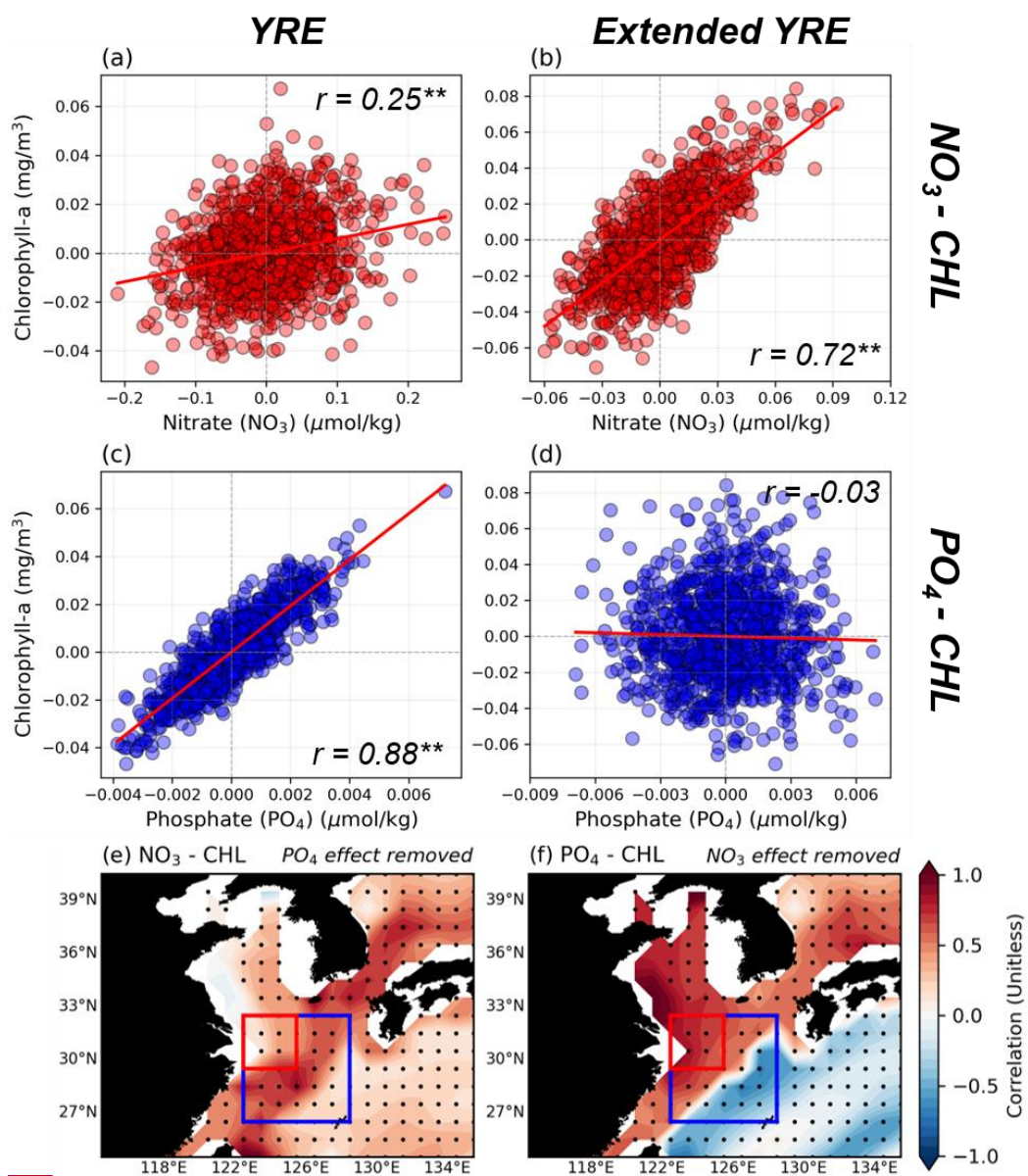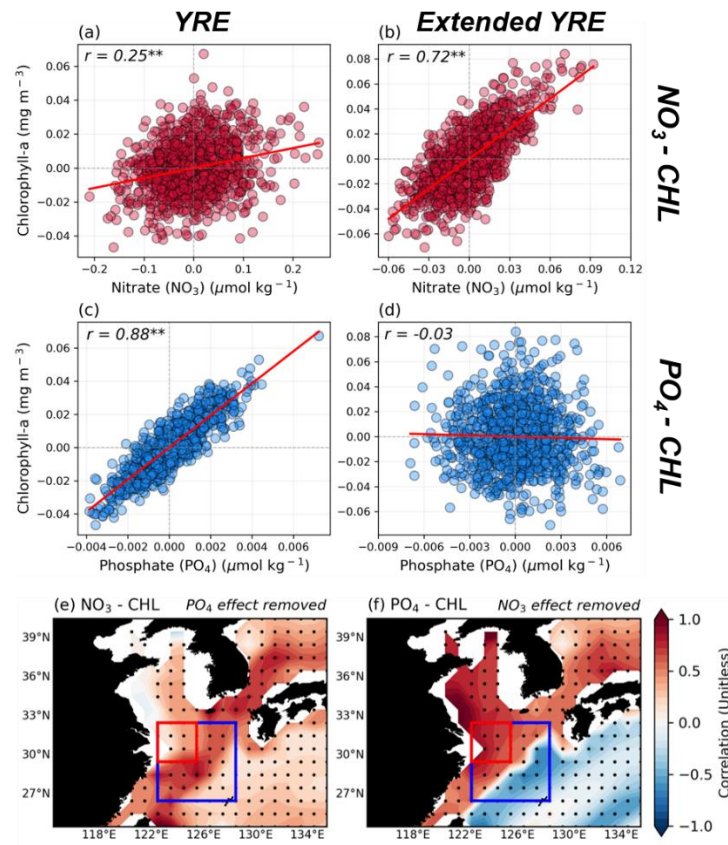
228 **Figure 2**. **(a-d)** The relationship between area-averaged surface nutrients and SCHL anomalies across the target
229 area. The upper panels (a-b) focus on the relationship between surface nitrate (NO_3) and SCHL anomalies in the
230 Yangtze River Estuary (YRE) [Left Panel; Fig. 2a] and extended YRE [Right Panel; Fig. ~~2b].~~2b] in model results.
231 The lower panels (c-d) indicate the relationship between surface phosphate (PO_4) and SCHL anomalies in YRE
232 [Left Panel; Fig. 2c] and extended YRE [Right Panel; Fig. 2d] within the ECS region respectively. **(e-f)** Partial
233 correlation distribution of the effect of surface NO_3 on SCHL anomalies after removing the effect of surface PO_4
234 and opposite case respectively. The red box and blue box with the excepted red box represent the YRE and
235 Extended YRE regions respectively.

236

237   Figures 3a-c present the composites of SCHL anomalies, surface NO_3, and surface PO_4 anomalies during

238 the decaying summer season following the mature phase of El Niño from all El-Niño cases in the GFDL-CM2.1

239 ESM model over a total period of 1,000 years. Unlike the satellite-observed SCHL anomalies shown in Fig. 1a

240 which are concentrated in the YRE region and gradually weakened outwards, the model results depict a diagonal

241 band pattern extending from the southeastern part of China to the Korean Strait (Figure 3a). This anomalous SCHL

242 pattern is somewhat consistent with the weak rightward diagonal pattern shown in Fig. 1a. Surface NO_3 anomalies

243 in Fig. 3b exhibit strong signals primarily in the YRE region, akin to the SCHL anomalies observed in Fig. 1a.

244 This similarity can be attributed to the ESM's ~~incorportation~~incorporation of N inputs from riverine runoff,

245 effectively capturing the observed patterns. In contrast, surface PO_4 anomalies (Figure 3c) show a diagonal shape

246 with a positive signal from the northeastern part of Taiwan to the Korean strait. Given that the ESM does not

247 include P input from riverine sources, ~~this anomalous PO₄ pattern can be driven by alternative processes. Therefore,~~

248 ~~it is essential to explore additional mechanisms for phytoplankton blooming beyond the runoff driven~~

249 ~~mechanisms~~these anomalous PO$_4$ patterns may result from nutrient supply through the TS. Additionally, nutrient

250 entrainment from subsurface waters via buoyancy upwelling induced by enhanced river discharge could further

251 support.

252
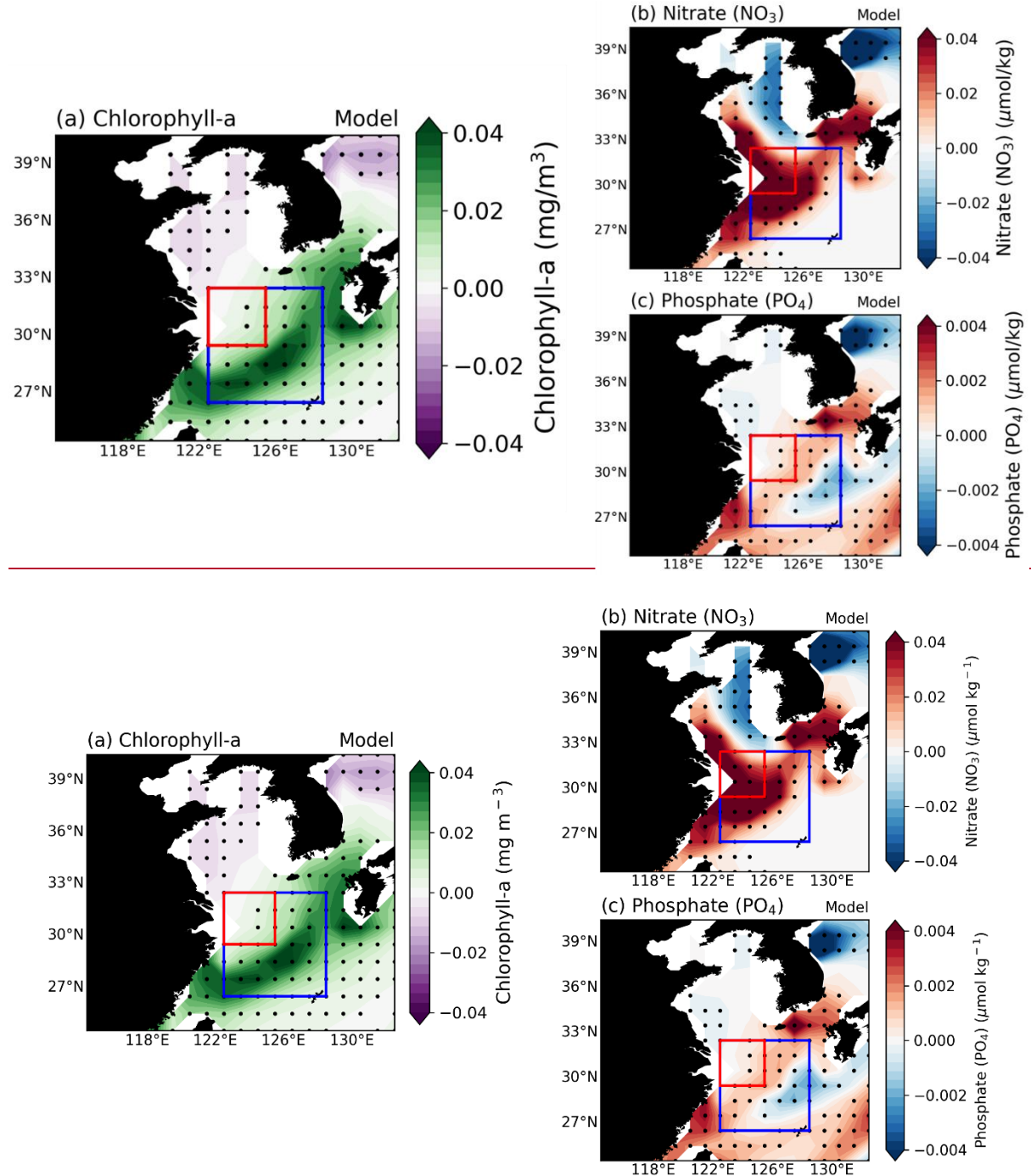
253 **Figure 3. (a-c)** Composite maps illustrate the SCHL, surface NO$_3$, and surface PO$_4$ distribution of El Niño

254 decaying summer season over the East China Sea (ECS) for all El Niño cases (176 years) which were selected in

255 GFDL-CM2.1 ESM results. All the black dots indicate where the responses are statistically significant at the 95%

256   confidence level, determined using the bootstrap method.

257

258   We examined the relationship between the DJF Niño3.4 index and SCHL anomalies in the ECS region,
259   showing a significant positive correlation (r = 0.51**) at the 99% confidence level (Figure 4a). From the long-
260   term integrated ESM results, we identified a total of 176 El Niño cases. Most of these cases result in positive
261   anomalous SCHL blooming, however, about 25% of the total El Niño cases exhibit negative SCHL anomalies. To
262   identify the processes responsible for the differing blooming outcomes, we divided the El Niño cases into two
263   groups based on the magnitude of anomalous SCHL blooming in the target region. The Strong Blooming (SB)
264   group, comprising the top 30 cases exhibiting strong blooming colored in reds, and the Non-Blooming (NB) group,
265   comprising the bottom 30 cases colored in blues (Figure 4b).
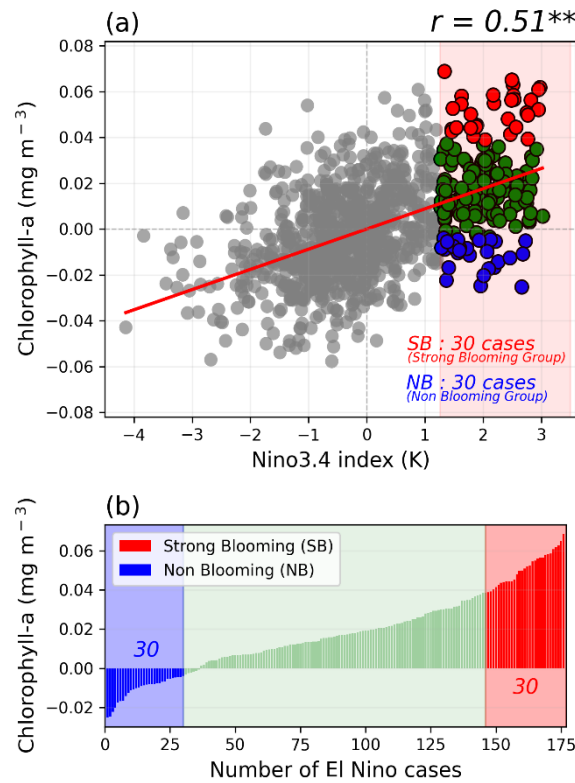
266   **Figure 4. (a)** The relationship between Niño3.4 DJF index and area-averaged SCHL anomalies over the target
267   region in GFDL-CM2.1 Earth System Model (ESM) during the El Niño decaying summers. Gray dots indicate
268   the Non-El Niño cases and colored dots indicate the El Niño cases. **(b)** Categorization of all El Niño cases by the
269   magnitude of SCHL blooming in the target region of the ECS during El Niño decaying summers. The top 30 and
270   bottom 30 cases, distinguished by SCHL anomaly magnitudes over the target region, colored in red and blue are
271   grouped into the Strong Blooming El Niño (SB) group and the Non-Blooming El Niño (NB) group, respectively.

272

273   The composite map of SCHL anomalies during the El Niño decaying summer of the SB group reveals
274   pronounced anomalous blooming across the ECS region, while the NB group is characterized by negative SCHL
275   anomalies (Figure 4b, Figs. S1a-c). Surface nutrient distributions from the composite maps also show contrasting

results between the two groups during the El Niño decaying summer (Figs. S1d-i). To investigate the runoff-driven phytoplankton blooming mechanism, as discussed in previous studies and above, we analyzed the composite patterns of precipitation and runoff anomalies during the El Niño decaying summer season by comparing the two groups (Figure 5). In terms of precipitation patterns, the SB group exhibits a broad positive rainfall band extending over the entire East Asia region, from central China to Japan. In contrast, the NB group shows only weak positive precipitation anomalies, confined to a narrow region of China, Taiwan, and the southern part of Japan. Similarly, the runoff anomaly patterns display positive signals centered on the YRE region and the northern part of the YRE region for both groups, with significance observed only in the SB group. The NB group, however, exhibits only weakly significant positive patterns around the southern part of the YRE region. Moreover, the relationship between runoff anomalies and the SCHL anomalies in the target region demonstrates a significantly positive correlation ($r = 0.59**$) at the 99% confidence level, indicating that the runoff-driven mechanism is well simulated in the model (Figure 5g).
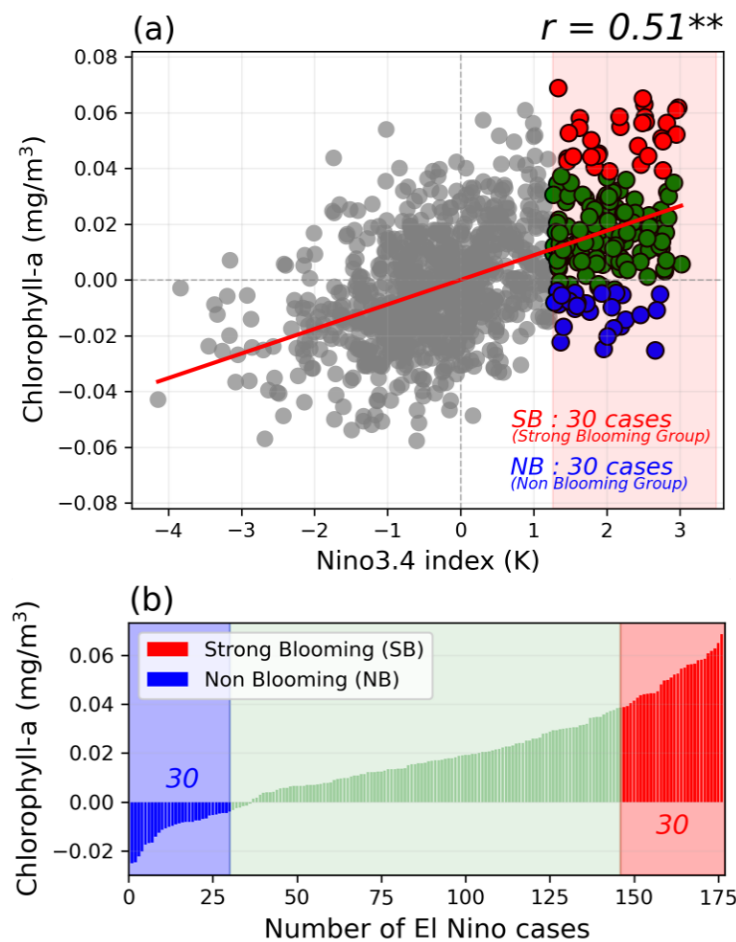
Figure 4. (a) The relationship between Niño3.4 DJF index and area averaged SCHL anomalies over the target region in GFDL CM2.1 Earth System Model (ESM).

291
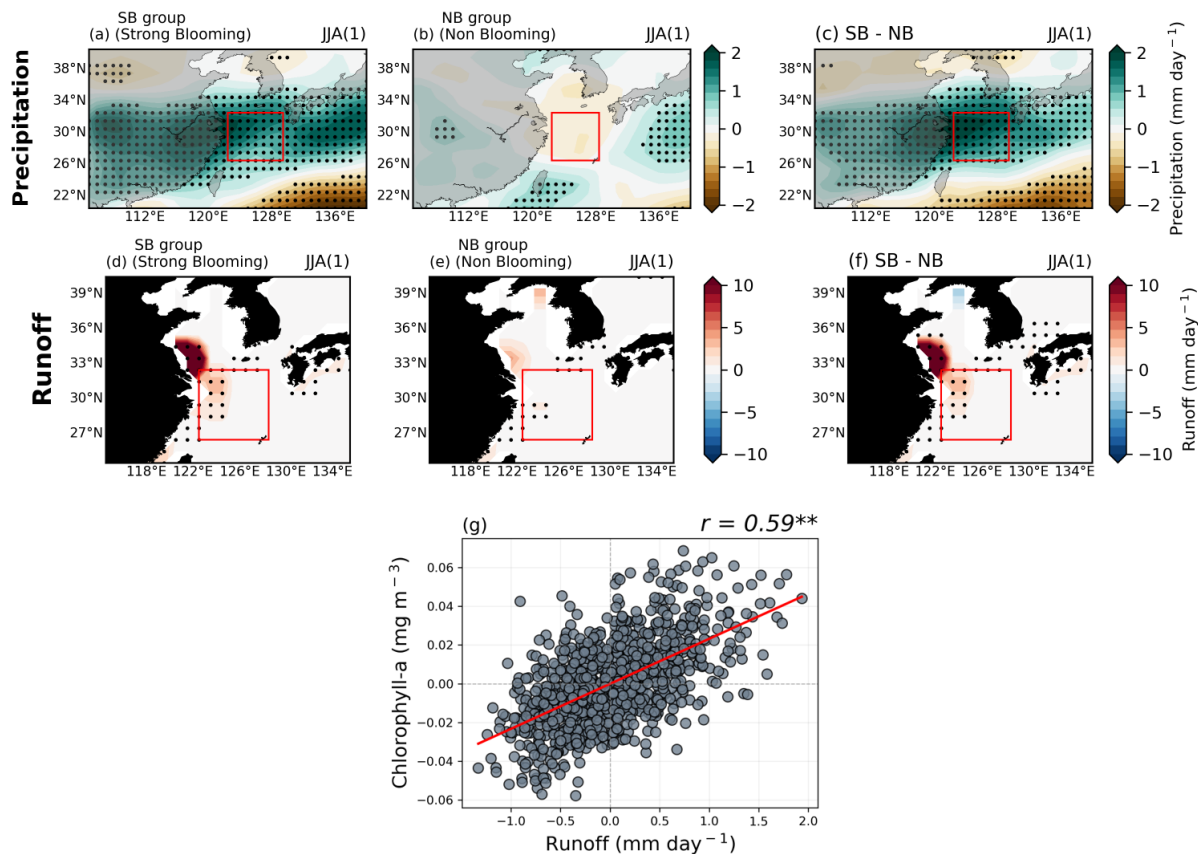
292 ~~(b) Categorization of all El Niño cases by the magnitude of SCHL blooming in the target region of the ECS~~
293 ~~during El Niño decaying summers. The top 30 and bottom 30 cases, distinguished by SCHL anomaly magnitudes~~
294 ~~over the target region, colored in red and blue are grouped into the Strong Blooming El Niño (SB) group and the~~
295 ~~Non Blooming El Niño (NB) group, respectively.~~
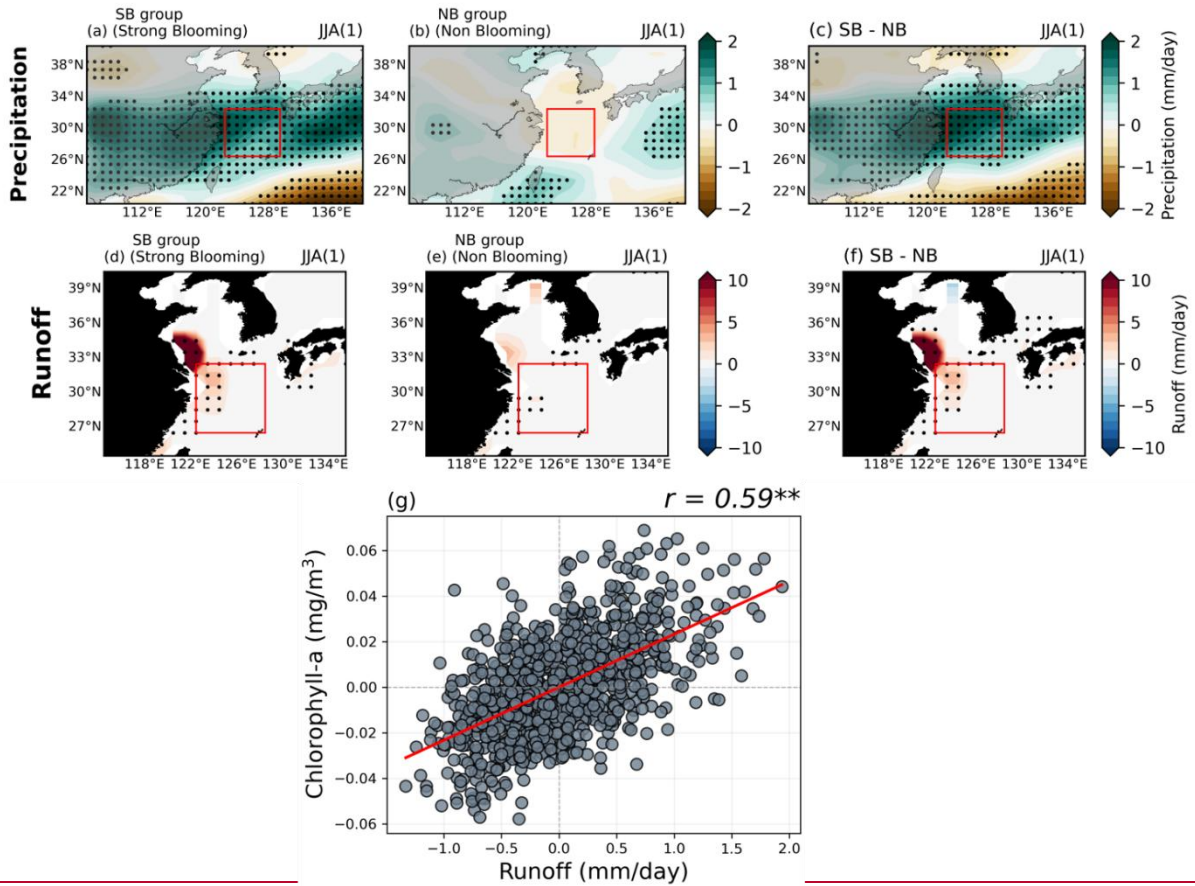
Figure 5. (a-c) Composite maps exhibiting precipitation anomalies during the El Niño decaying summer season for both groups, as well as the difference between the two groups. **(d-f)** Similar to Figs. 5a-c, these maps demonstrate a composite map of runoff anomalies during the El Niño decaying summer season for both groups, as well as the difference between the two groups. **(g)** The relationship between area-averaged runoff and SCHL anomalies over the target region. All figures show the GFDL-CM2.1 model results.

We also investigated the TS-transport-driven blooming mechanism, which is well known for its significant role in nutrient supply through the TS. We analyzed the meridional PO_4 transport by comparing two groups as the same as Fig. 5, and found remarkably distinct differences between them (Figure 6a-c). Notably, within the TS, a strong positive (negative) signal was identified in the SB (NB) group. For the SB group, the nutrient flux exhibits a significant positive signal reaching the target region, potentially supplying large amount of nutrients and making a substantial contribution to SCHL blooming in the ECS region. Furthermore, a positive correlation of 0.68—higher than the runoff-driven mechanism—was identified between the anomalous SCHL blooming magnitude in the target region and the meridional PO_4 transport index indicated by the blue diagonal box in the TS region (Figure. 6d). This underscores the critical role of the TS-transport-driven mechanism in

312   fostering nutrient into the ECS region.

313
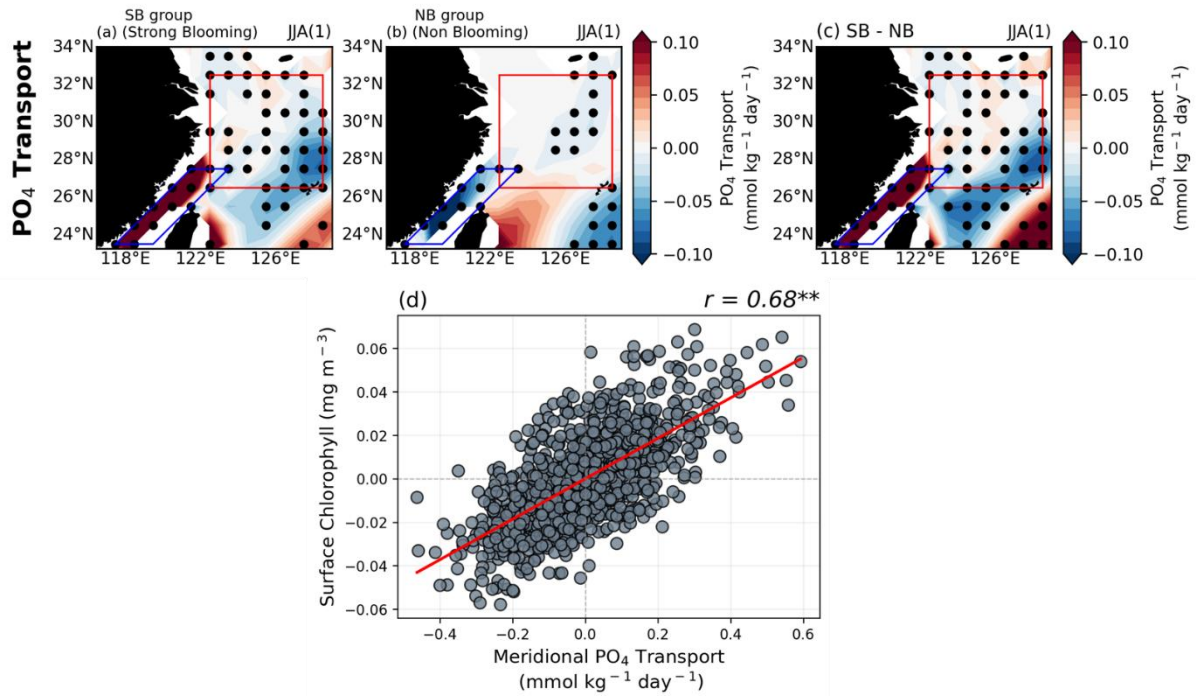
314   **Figure 6. (a-c)** Composite maps exhibiting meridional PO$_4$ transport anomalies during the El Niño decaying
315   summer season for both groups, as well as the difference between the two groups. **(d)** The relationship between
316   area-averaged meridional PO$_4$ transport and SCHL anomalies over the target region. All figures show the GFDL-
317   CM2.1 model results.

318

319   **3.3. Upwelling-driven blooming mechanism - Insight from Model**

320   In addition to ~~precipitation and~~ runoff-driven and TS-transport-driven mechanisms, there was a
321   distinctive difference in the magnitude of upwelling between the two groups. ~~Figures 6a-b show~~Figure 7 shows
322   the composite map of Ekman Upwelling (EKU) anomalies during the El Niño decaying summer season. For the
323   SB group, a ~~significant~~significantly positive EKU pattern dominates the ECS region, with significantly negative
324   EKU distribution in the WNP region, far south of Japan (Figure ~~6a~~7a). On the other hand, the NB group does not
325   exhibit any significant EKU anomaly patterns in the target region, with significant positive EKU patterns over the
326   southern part of Japan and negative EKU anomalies in the WNP but without significance (Figure ~~6b~~7b). The
327   difference between the two groups highlights distinct EKU anomaly patterns in the target region (Figure ~~6c~~7c).
328   The intensified EKU in the target region facilitates the ~~transport~~supply of abundant nutrients from the subsurface
329   layer to the surface layer, thereby enhancing phytoplankton growth. This is supported by the significantly positive
330   correlation (r = 0.47**) at the 99% confidence level between EKU anomalies and SCHL anomalies in the target
331   region, indicating that EKU can significantly contribute to anomalous phytoplankton blooming~~, similar to the~~
332   ~~runoff driven mechanism~~ (Figure ~~6d~~7d).

333   EKU is primarily generated by cyclonic atmospheric circulations. The presence of robust upwelling in

the ECS region signifies the formation of cyclonic circulation, i.e. the EKU and wind stress curl (WSCL) are fully positively correlated (Fig. S2a). During the El Niño mature phase, suppressed convection in the western Pacific induces the Western North Pacific Anticyclone (WNPAC) in the lower-troposphere structure ~~(Gill, 1980; Matsuno, 1966).~~(Gill, 1980; Matsuno, 1966; Xie et al., 2016; Chowdary et al., 2019). Moreover, the WNPAC leads to cyclonic circulation in the northwestward ECS region via low-level Rossby wave energy propagation (Wang et al., 2000). This sequence of wave patterns in the lower troposphere can generate ~~the WNPAC and atmospheric~~ cyclonic circulation in the ECS region during the El Niño decaying summer seasons. ~~Given the significant differences in the magnitude and extent of rainfall band between the two groups, we would expect distinct differences in the growth of WNPAC between the two groups as well. This suggests that the differences in WNPAC development contribute to the variability in EKU and, consequently, the extent of phytoplankton blooming in the ECS region during El Niño decaying summers.~~
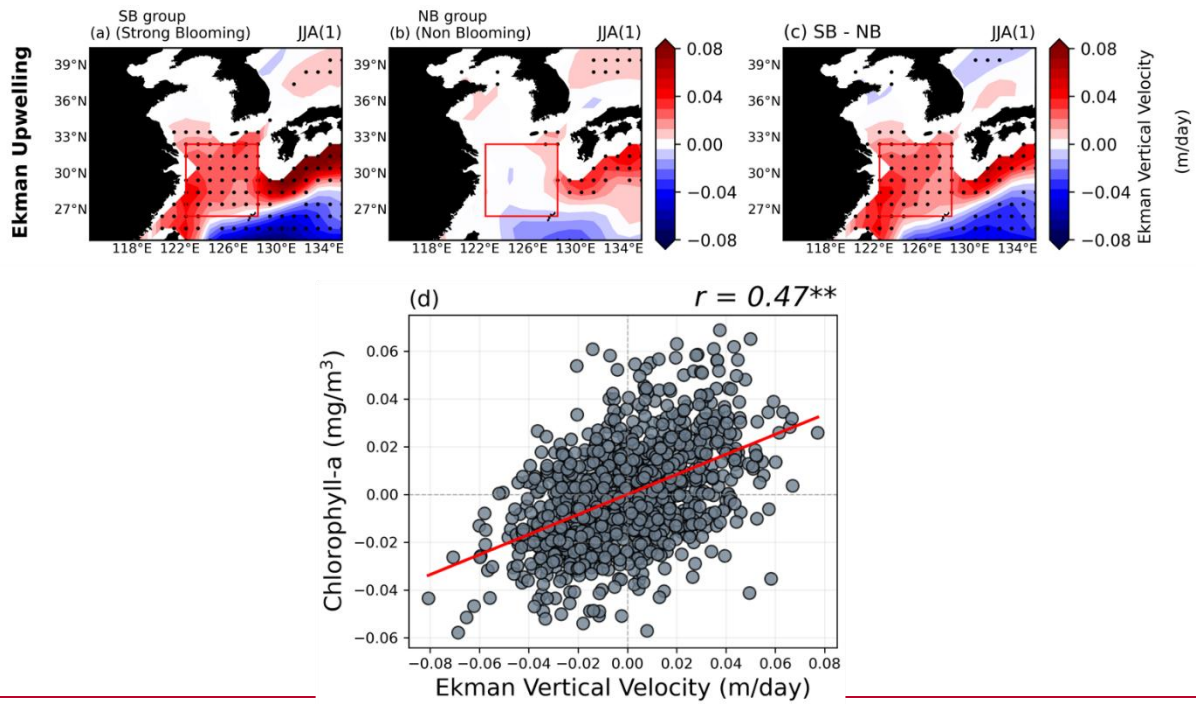
Figure 6. (a-c) ~~Composite maps exhibiting Ekman Upwelling (EKU) anomalies during the El Niño decaying summer season for both groups, as well as the difference between the two groups.~~ **(d)** ~~The relationship between area averaged EKU and SCHL anomalies over the target region.~~
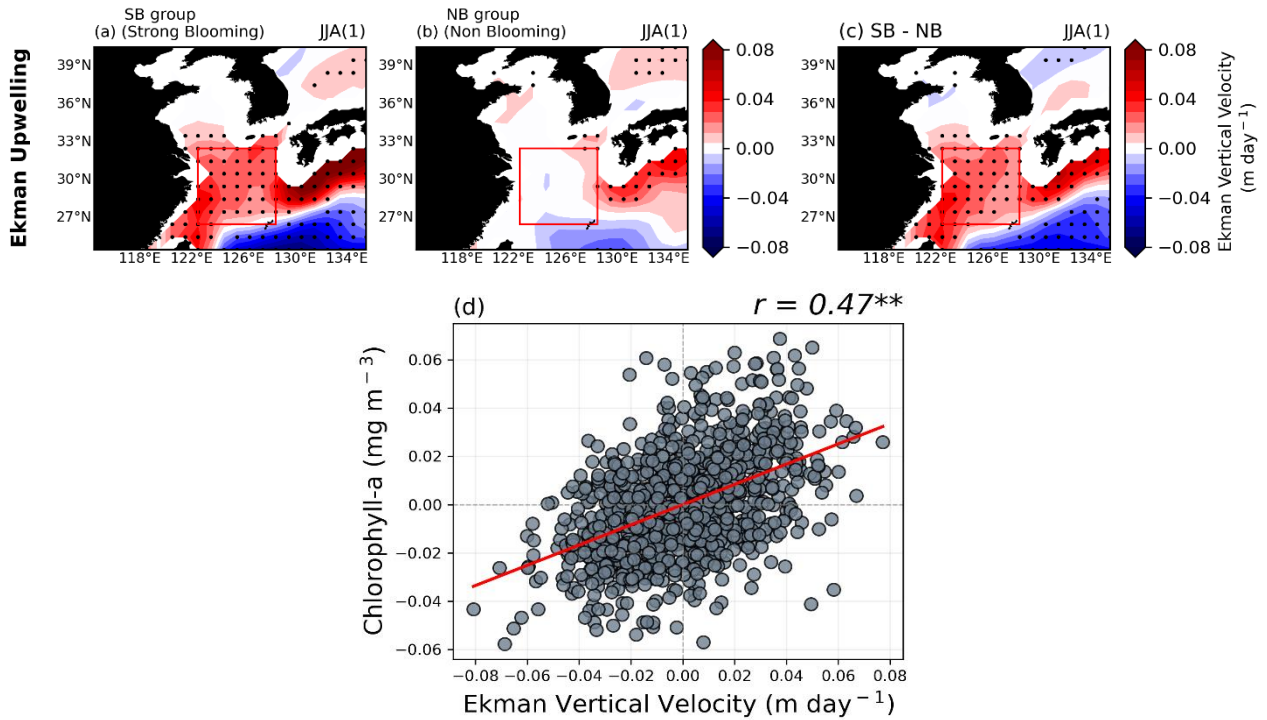
Figure 7. (a-c) Composite maps exhibiting Ekman Upwelling (EKU) anomalies during the El Niño decaying summer season for both groups, as well as the difference between the two groups. **(d)** The relationship between area-averaged EKU and SCHL anomalies over the target region. All figures show the GFDL-CM2.1 model results.

Given the Rossby wave teleconnection pattern, it is expected that the EKU response can be related to the strength of the WNPAC. Figure 8 illustrates the evolution of geopotential height (GPH) differences with 850hPa wind (Left panels) and WSCL anomalies (Right panels) between two groups in the WNP across three seasons (D(0)JF(1)-MAM(1)-JJA(1)) following El Niño mature phase. In the SB group, the WNPAC and North Pacific Cyclone (NPC) are prominently stronger, positioned over the Philippines and North Pacific, respectively (Figure 7a8a). These atmospheric circulations result in anomalous positive WSCL around the Korean Peninsula, Japan, and East Sea, while negative WSCL is observed in southeastern of China (Figure 7d8d). As the seasons progress, the WNPAC migrates northeastward, becoming more pronounced in the SB group compared to the NB group, continuing into the subsequent summer (Figures 7b8b-c). Positive WSCL anomalies begin to emerge in the ECS region from El Niño decaying spring season, coinciding with the developed WNPAC (Figure 7e8e). By summer, the WNPAC in the SB group is intensely and broadly developed, dominating the WNP, leading to a stronger cyclonic circulation in the ECS region and enhanced wind-driven EKU due to positive WSCL (Figure 7e8c and Figure 7f8f). The correlation between WSCL and the WNPAC index with slight broader than observations (13.5°N–26.5°N / 124.5°E–160.5°E; which is slightly broader than observations) calculated from GPH anomalies within the red box in Fig. 7g8c exhibits a significantly positive relationship (r = 0.45**) at the 99% confidence level. This implies that the development of a stronger WNPAC may lead to the generation of

368 anomalous positive WSCL, prompting upwelling and facilitating anomalous phytoplankton blooming during El

369 Niño decaying summers.

370
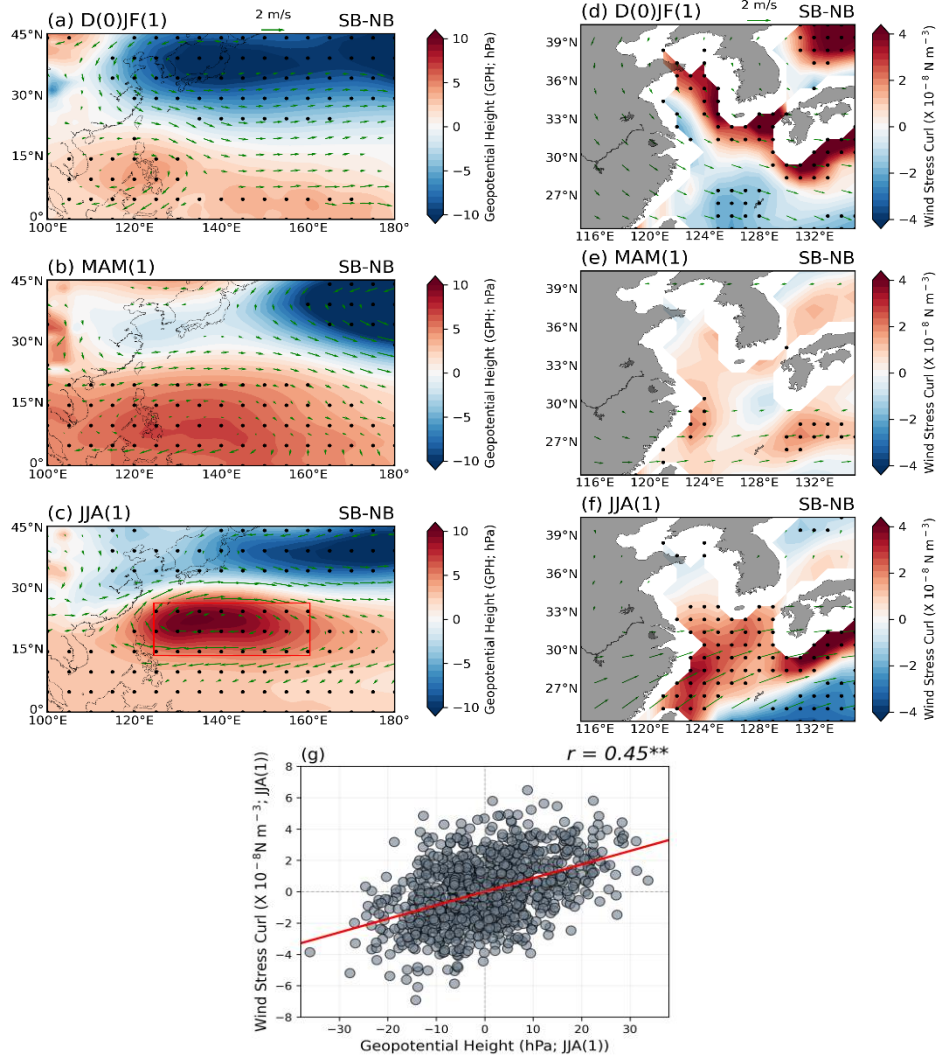
Figure 8. Evolution map of El Niño composite of (a-c) geopotential height (GPH; Left panels) and (d-f) Wind Stress Curl (WSCL; Right panels) with 850hPa wind anomalies (vectors) from El Niño mature phase to decaying summer season for the differences between two groups. All the black dots indicate where the responses are statistically significant at the 95% confidence level, determined using the bootstrap method. (g) The relationship between area-averaged Western North Pacific (WNP) GPH anomalies (highlighted as a red box in Fig. 8c) and Wind Stress Curl (WSCL) anomalies over the target region during the summer season. All figures show the GFDL-CM2.1 model results.
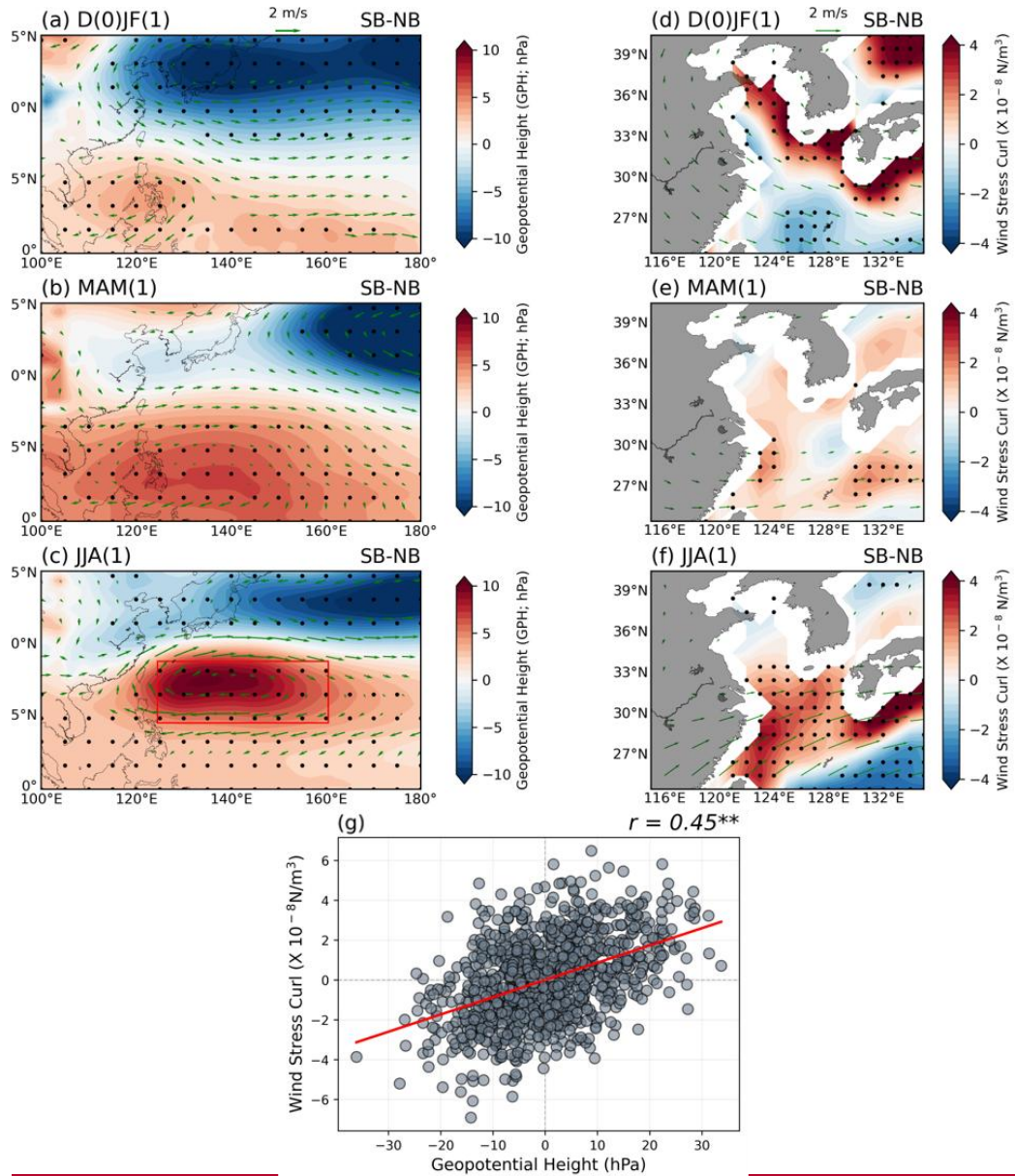
Figure 7. ~~Evolution map of El Niño composite of~~ **(So far, we have conducted** a ~~c)~~ geopotential height (GPH; ~~Left panels)~~ **comprehensive evaluation** and ~~(d-f)~~ Wind Stress Curl (WSCL; Right panels) with 850hPa wind ~~anomalies (vectors) from El Niño mature phase to~~ **analysis of the complex mechanisms driving phytoplankton blooms in the ECS during the summers following the** decaying ~~summer season for the differences between~~ ~~two groups.~~ **(g)** ~~The relationship between area averaged Western North Pacific (WNP) GPH anomalies~~ ~~(highlighted as a red box in Fig. 7c) and Wind Stress Curl (WSCL) anomalies over the target region. All the black~~ ~~dots indicate where the responses are statistically significant at the 95% confidence level, determined using the~~ ~~bootstrap method.~~

~~As shown in Fig. 5 and Fig. 6, both~~ phase of El Niño events. In addition to the runoff- and TS-transport-driven ~~and~~ mechanisms suggested in previous studies, we introduced the Ekman upwelling-driven ~~mechanisms~~ ~~work to contribute to the strong~~ blooming ~~observed in the SB group. To quantify~~ mechanism. Subsequently, we quantified the relative contributions of these ~~mechanisms, we applied partial correlation and joint composite~~

384 ~~analyses. The partial correlation analysis revealed that the impact of the runoff-driven mechanism on~~
385 ~~phytoplankton blooming, after removing the effect of the upwelling-driven mechanism, is 0.49**. Conversely, the~~
386 ~~effect of the upwelling-driven mechanism on phytoplankton blooming, after accounting for the runoff-driven~~
387 ~~mechanism, is 0.31**. These results indicate that while both mechanisms play significant roles, the runoff-driven~~
388 ~~mechanism has a relatively stronger influence.~~ three mechanisms based on regression methods using (Eq. 4) as
389 follows:

390 ~~Additionally, the joint composite analysis further demonstrated that both mechanisms contribute to~~
391 ~~anomalous phytoplankton blooming. We performed this analysis by assessing the relative strengths of runoff and~~
392 ~~WSCL in the target region (Figure 8a). We categorized the 176 El Niño cases into four groups based on whether~~
393 ~~the runoff and WSCL anomalies were positive or negative during the decaying summer season of El Niño events~~
394 ~~(Figure 8b). The results showed that 62% (109 cases) of the El Niño cases exhibited both positive runoff and~~
395 ~~WSCL anomalies. Furthermore, 13% (22 cases) and 11% (19 cases) displayed positive anomalies for either WSCL~~
396 ~~or runoff, respectively, while 15% (26 cases) were negative for both. The magnitude of anomalous blooming was~~
397 ~~highest when both WSCL and runoff anomalies were positive. The average blooming magnitude when WSCL~~
398 ~~was positive but runoff anomalies were negative was almost the same, with little weakness of about 8% (0.0007~~
399 ~~mg m⁻³) compared to vice versa. When both were negative, the blooming magnitude was negative on average.~~
400 ~~Importantly, a statistically significant positive blooming magnitude was observed only when both mechanisms~~
401 ~~were positively contributing. Therefore, the combined effect of both mechanisms is crucial for the anomalous~~
402 ~~phytoplankton blooming observed in the ECS region during the El Niño decaying summers.~~

403

404
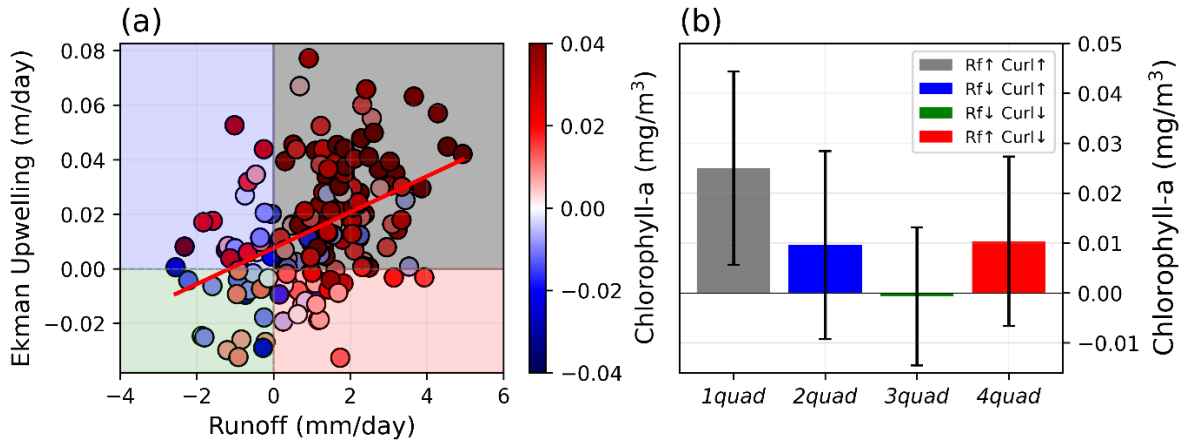
405 **Figure 8. (a)** ~~The scatter plot indicates the runoff and wind stress curl in the target region during the following~~
406 ~~summer season of all El Niño cases selected from the GFDL-CM2.1 ESM. Colored scatters show the anomalous~~
407 ~~blooming magnitude in the target region.~~ **(b)** ~~Bar plots indicate the averaged anomalous blooming magnitude of~~
408 ~~the selected El Niño cases of each quadrant in Fig. 8a over the target region. Crosses indicate the range of ±1~~
409 ~~standard deviation.~~

410

$$\frac{dChl}{dNino3.4}(\alpha) = \frac{\partial Chl}{\partial Runoff} \times \frac{dRunoff}{dNino3.4} + \frac{\partial Chl}{\partial TS-transport} \times \frac{dTS-transport}{dNino3.4} +$$

411

$$\frac{\partial Chl}{\partial Ekman-Upwelling} \times \frac{dEkman-Upwelling}{dNino3.4} + residual \qquad (4)$$

412

413 Firstly, we normalized all variables and conducted the multiple regression with respect to SCHL index
414 in the target region as the dependent variable and three mechanism indices as independent variables. Secondly,
415 we calculated each term by multiplying the linear regression coefficient between Nino3.4 index and each
416 mechanism index by the corresponding multiple regression coefficient for each mechanism index. The combined
417 effects of the three mechanisms and the residual term collectively account for the variation of the SCHL index in
418 the ECS region with respect to the El Niño events. Therefore, each term indicates how changes in three mechanism
419 induced by ENSO cycle (as indicated by the Nino3.4 index) affect on phytoplankton blooms in the ECS region.
420 The results show the effect of runoff-driven mechanism and the TS-transport mechanisms to SCHL blooming
421 intensity in the target region are comparable (Table 1). In the case of the Ekman upwelling mechanism, it accounts
422 for about 40% to 47% of contributions comapred to the other two mechanisms, yet still exerts a meaningful
423 influence as well.

424 **Table 1.** Relative contributions of three mechanisms to SCHL blooming in the target region.

	α	Runoff	TS-transport	Ekman Upwelling
Contribution	0.511	0.152	0.138	0.065

425 Additionally, we identified their spatial contributions to further elucidate the effects of each mechanism
426 within the target region (Figure 9). We conducted multiple regression for three mechanism indices at each grid
427 point of SCHL anomalies across the target region. Following the same way examined above, we calculated the
428 spatial contributions by multiplying the linear regression coefficents of each mechanism with repsect to the
429 Nino3.4 index. The results showed that the runoff-driven mechanism exhibited the strongest contribution at the
430 center of the target region, driven by direct riverine nutrient inflow (though the model doesn't simulate P input)
431 and nutrient supply through buoyancy upwelling induced by river discharge (Figure 9a). In contrast, the TS-
432 transport-driven mechanism significantly contributes along a southwest-northeast diagonal direction, aligning
433 with nutrient transport via the TS from the SCS (Figure 9b). Additionally, the newly proposed Ekman upwelling-
434 driven mechanism, while relatively lower in overall contribution, shows significant and uniformly distributed
435 impacts across the target region (Figure 9c). These results suggest that all mechanisms can affect comprehensively
436 to induce phytoplankton blooms in the ECS during the following summers of the decaying phase of El Niño events.
437 Therefore, considering all mechanisms is essential for accurately predicting the intensity of phytoplankton blooms.

438
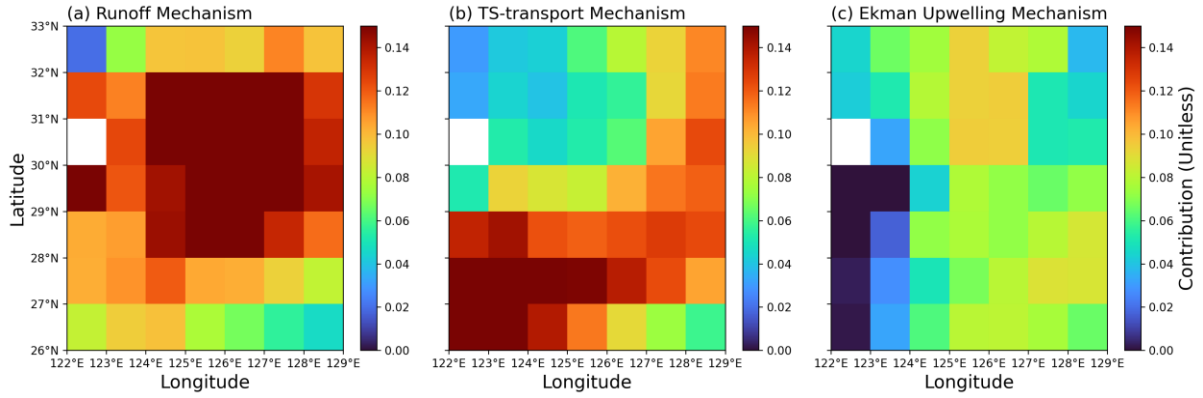
Figure 9. Relative contributions of three mechanisms to SCHL blooming in the target region during summers following the decaying phase of El Niño events **(a)** Runoff-driven mechanism **(b)** TS-transport-driven mechanism **(c)** Ekman upwelling-driven mechanism. All figures show the GFDL-CM2.1 model results.

3.4. Upwelling-driven blooming mechanism - Insight from Observations

~~So far, we have re-evaluated the runoff-driven mechanism using model results and identified an upwelling-driven mechanism.~~ Lastly, we examined the upwelling-driven mechanism using reanalysis data for physical variables and chlorophyll-a satellite data to verify its application to the real world. Figure ~~9a~~10a shows the composite map of GPH anomalies during the El Niño decaying summer, using NCEP2 re-analysis data. To identify the typical WNPAC and 850hPa wind anomalies during El Niño decaying summers, we defined a WNPAC index using the full period of available NCEP2 re-analysis data (1979-2022; 44 years). The WNPAC index was defined as the area-averaged (16.5°N-26.5°N, 130°E-155°E) GPH anomalies over the WNP region indicated by the red box in Fig. ~~9a~~10a. The WNPAC pattern and anticyclonic 850hPa wind anomalies ranging from the South China Sea to the WNP, are well represented in the re-analysis data. We calculated the WSCL using surface winds from the NCEP2 re-analysis data, revealing significant positive WSCL (cyclonic circulation) anomalies over a large area of southeastern China (Figure ~~9b~~10b). Furthermore, we found a significant positive correlation (r = 0.56**) at the 99% confidence level between the WSCL index (red box in Fig. ~~9b~~10b) and SCHL anomalies in the target region (Figure ~~9c~~10c). Additionally, there is a significant positive correlation (r = 0.43*) at the 95% confidence level between the WNPAC index and the SCHL anomalies in the target region (Figure ~~9d~~10d). A strong positive relationship (r = 0.56**) at the 99% confidence level between the WNPAC index and WSCL in the target region was also observed (Figure ~~9e~~10e). Several instances of negative SCHL anomalies occurred despite positive anomalous rainfall (blue box in Fig. ~~9a~~10a; 28.5°N-33.5°N, 111°E-120°E). However, interestingly, cases exhibiting strong anomalous SCHL blooming mostly coincided with either strong WNPAC indices or robust cyclonic WSCL in the ECS region (Figure ~~9e~~10e). These remarkable associations among these variables suggest that the upwelling-driven blooming mechanism is indeed operating in the real world. Therefore, ~~both~~all of the ~~runoff-driven and~~mechanisms suggested in this study including upwelling-driven mechanisms must

466   be considered together to fully understand the dynamics of phytoplankton blooming in the ECS region during El

467   Niño decaying summers.

468
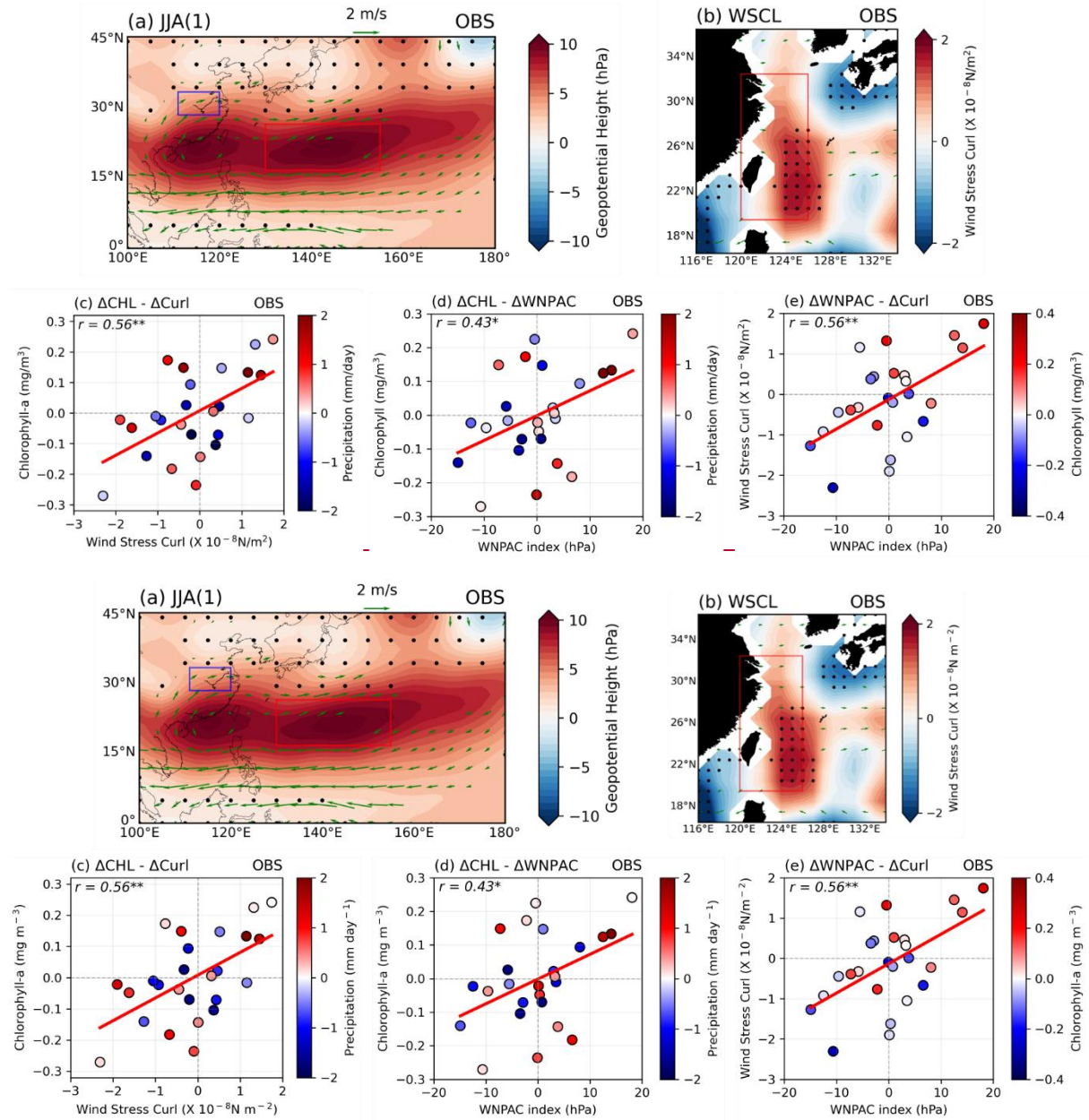
471   **Figure 910. (a)** The composite map exhibits the GPH anomalies over the WNP and 850hPa wind anomaly patterns

472   during the El Niño decaying summer season for the available period of re-analysis data (1979-2022; 44 years).

473   Red and blue boxes indicate the area-averaged WNPAC index (16.5°N-26.5°N, 130°E-155°E) and precipitation

474   index (28.5°N- 33.5°N, 111°E-120°E) respectively. Black dots indicate the insignificance at the 90% confidence

475   level using the bootstrap method. **(b)** The composite map shows WSCL anomaly patterns and 850hPa wind

476   anomaly patterns during the El Niño decaying summer season within the same period with Fig. 9a10a. The red

477   box indicates the area-averaged WSCL index. Black dots indicate the significance at the 90% confidence level

478   using the bootstrap method. **(c-d)** The relationship between SCHL anomalies in the target region and the WSCL

479   index and the WNPAC index respectively. Colored scatters show the precipitation index over the eastern part of
480   China. **(e)** The relationship between the WNPAC index and the WSCL index. Colored scatters show the magnitude
481   of SCHL anomalies in the target region.

4. Discussions

This study investigates the comprehensive mechanisms of anomalous phytoplankton blooms in the ~~East China Sea~~ECS region during the summer following El Niño events. We re-evaluated the existing runoff-driven and TS-transport-driven phytoplankton blooming mechanism using the observational data and long-term integrated ESM results based on present climate conditions. Notably, the ESM we used does not simulate P riverine input, a crucial factor in the YRE region, our research target region. Despite the absence of P riverine inputs, significant positive phytoplankton blooms still emerged, we hence proposed an additional mechanism to trigger anomalous phytoplankton blooming during the summers following the El Niño mature phase.

Firstly, we sorted all El Niño cases selected from long-term climate simulation results based on the magnitude of SCHL blooming in the ECS region and classified the El Niño cases into two groups (SB & NB group). There were clear differences between the two groups in climatic factors such as precipitation ~~and~~, runoff, and meridional PO_4 transport along TS pathway which drive ~~existing~~ blooming mechanisms commonly. In the SB group, stronger and broader rainfall band and riverine inputs into the ECS region were significantly predominant. The rainfall band generated over East Asia during the summer season of post-El Niño is related to the development of the WNPAC, suggesting that the WNPAC is more potently advanced in the SB group. Moreover, in the SB group by the enhanced development of WNPAC, the anomalous southwesterly winds associated with the SCS drive a pronounced augmentation of northward nutreint-rich water transport through the TS.

In addition, distinct differences between the two groups were observed, evident in both the magnitude of EKU anomalies induced by atmospheric circulation and the WSCL anomaly patterns. Consequently, We found a more robust and expansive WNPAC that persisted and extended its influence until the summer season, impacting a broader area of East Asia in the SB group. This well-developed WNPAC triggers stronger wind anomalies in the target region, leading to active EKU with positive WSCL. It facilitates upwelling in the water column as the cyclonic atmospheric circulation, driven by the strong clockwise circulation over WNP, prevailed across the entire ECS region.

Lastly, we validated the upwelling-driven phytoplankton blooming mechanism elucidated by the model results using reanalysis data and satellite chlorophyll-a data. There was a significantly positive relationship between WNPAC and SCHL anomalies, as well as WNPAC and WSCL anomalies in the target region. Thus, depending on the development of WNPAC during the El Niño decaying summers, anomalous phytoplankton blooms can be triggered by a conjunction of ~~different~~complex mechanisms: runoff-driven accompanied by strong precipitation in the ECS region, and TS-transport-driven by enhanced nutrient-rich water transport from SCS to ECS region through TS, as well as upwelling-driven mechanism induced by positive WSCL and EKU.

We investigated that the more vigorous development and expansion of the WNPAC can influence the marine ecosystems of the ECS region with sufficient El Niño cases using ESM results. The intensity and extent of WNPAC development between the SB and NB groups were distinct, which means that anomalous phytoplankton blooming can be predicted as early as two seasons before it occurs during the El Niño mature phase. We found a significantly positive lagged relationship between the WNPAC index and blooming magnitude in the

519 ECS region in both observations and ESM results (Figure ~~10).~~11a-d; Observations, Figure 11e-h; Model). There

520 were significant 2 seasons (D(0)JF(1) – JJA(1)) lagged positive correlations (r = 0.61**) and ESM results (r =

521 0.5**). In addition, the case of a short-term, 1 season lagged relationship (MAM(1) – JJA(1)) has higher lagged

522 positive correlations in both observations (r = 0.69**) and ESM results (0.57**) at the 99% confidence level.

523 These results demonstrate that the magnitude of WNPAC during the El Niño mature phase can be a good predictor

524 of the magnitude of phytoplankton blooms in the ECS region during the following summers of El Niño events.

525 ~~The present climate-based long-term integrated ESM (GFDL-CM2.1) utilized in this study, possesses a~~

526 ~~relatively low spatial resolution, leading to coarse representations of features like continental shelves and slopes~~

527 ~~like those in the YECS region. This limitation may hinder the accurate depiction of regional currents and local~~

528 ~~eddies, which are crucial for understanding ocean circulation dynamics, including the intrusion of the Kuroshio~~

529 ~~current near the north-eastern part of Taiwan Island, as mentioned in previous studies (Chen, 1996; Chen et al.,~~

530 ~~1995; Lee et al., 2023). However, since we are arguing for an upwelling mechanism in the ocean driven by~~

531 ~~atmospheric circulation rather than horizontal transport, the resolution limitation may not significantly impact our~~

532 ~~findings. Furthermore, our~~Our analyses are based on the present climate-based long-term integrated ESM, and

533 there may be changes in the pattern of WNPAC development due to changes in the ENSO teleconnection resulting

534 from changes in the El Niño mean state under global warming scenarios ~~(Kim et al., 2024; Shin et al., 2022; Yang~~

535 ~~et al., 2022; Yeh et al., 2009).~~(Yeh et al., 2009; Shin et al., 2022; Yang et al., 2022; Kim et al., 2024; Wang et al.,

536 2023). Here, we primarily focused on the biological aspect of the phytoplankton blooming mechanism and did

537 not extensively explore the dynamic mechanisms driving differences in WNPAC development intensity between

538 the two groups. In Fig. S3, we identified differences in the decaying speed of the El Niño strength between the

539 two groups and the warmer SST anomalies in the Central Pacific (CP) region during El Niño mature phase in the

540 SB group. Therefore, further studies will be necessary to investigate the blooming magnitude variations associated

541 with different El Niño types such as CP and Eastern Pacific (EP) El Niño (Kug et al., 2009, 2010; Yuan and Yang,

542 2012). Moreover, ~~Xie et al~~Xie et al (2009) mentioned that the anomalous large-scale anti-cyclone in the WNP

543 during the summer season of the El Niño decaying is associated with the Indian Ocean (IO), named the IO

544 Capacitor theory. These dynamic aspects will require further detailed exploration in subsequent studies.

545 Additionally, quantitative analyses between ~~runoff driven and upwelling driven~~all of the suggested blooming

546 mechanisms through model experiments will be necessary to provide a detailed understanding of the contribution

547 of ~~both~~all mechanisms to phytoplankton blooms during the El Niño decaying summer season.
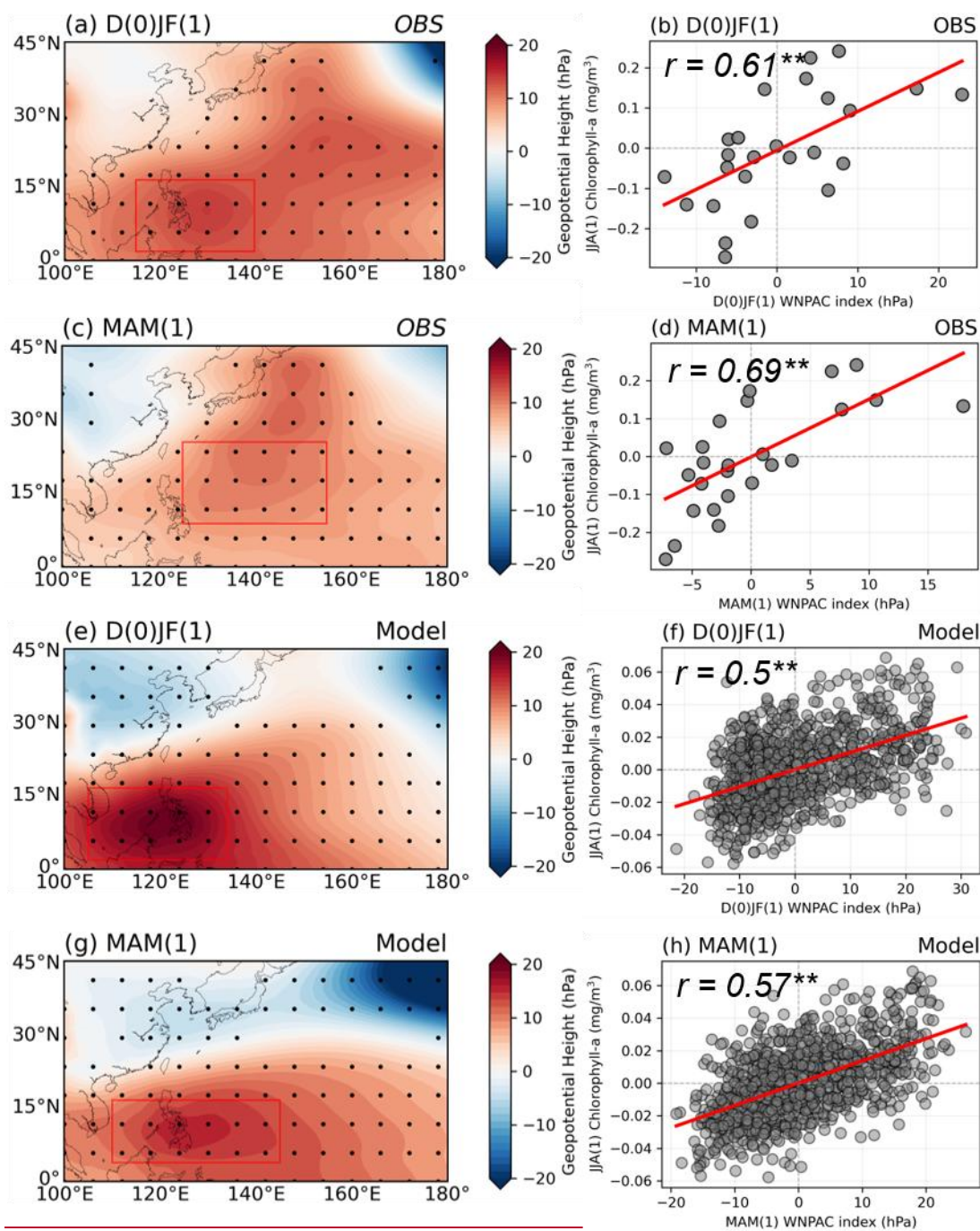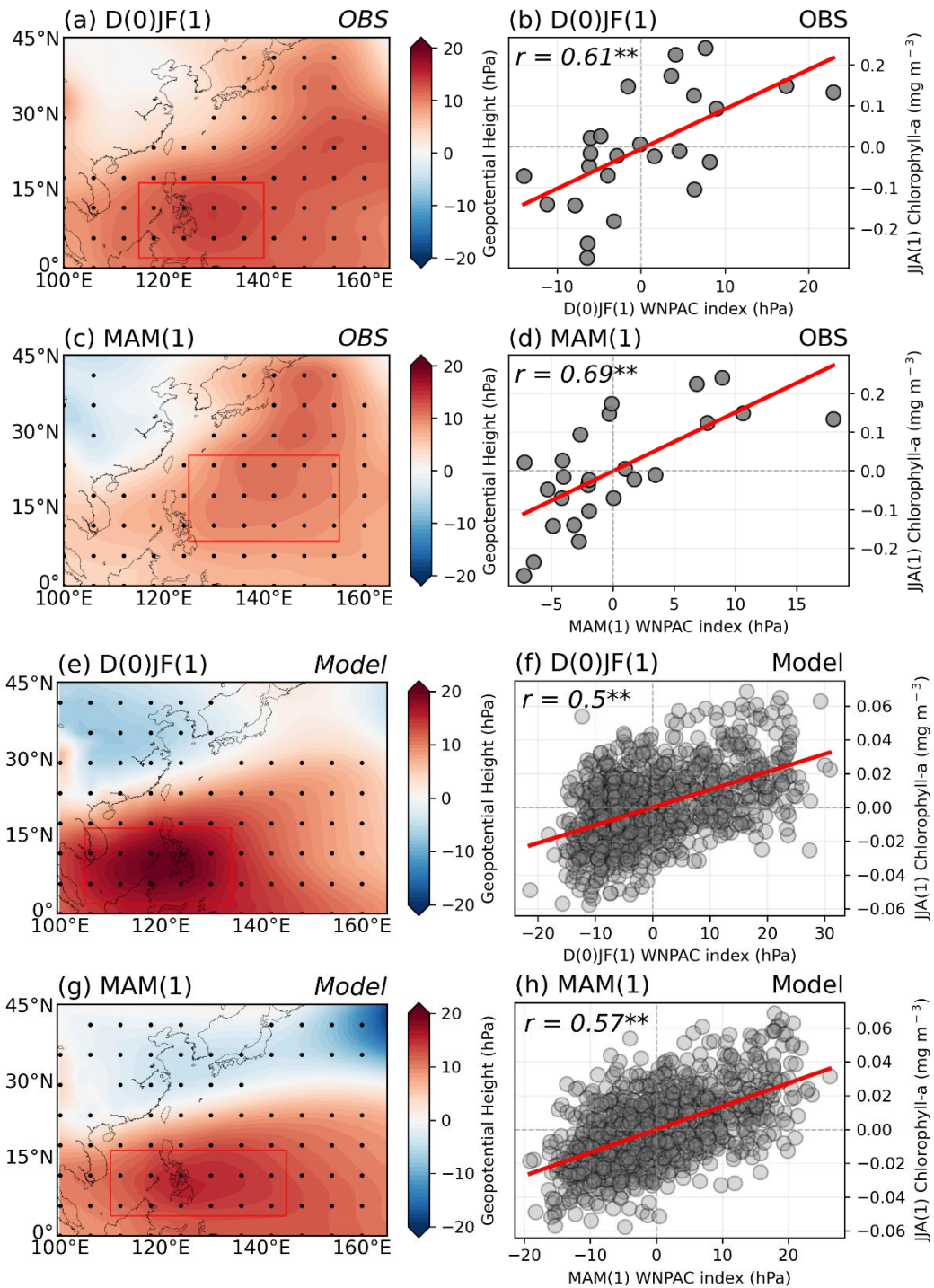
Figure ~~10~~11. (a-d) Evolution maps indicate the distribution of GPH anomalies from the mature phase (D(0)JF(1)) of El Niño to the following spring season (MAM(1)) in the observations. Scatter plots show the lagged relationship between the area-averaged WNPAC index (red box in the left panels) during each period and the anomalous SCHL blooming magnitude in the target region during the decaying summers of the El Niño in observations. **(e-h)** Same as (a-d), but with model results.

Data availability

The chlorophyll satellite observation data used in this study is available on https://esa-oceancolour-cci.org. The ERSST (SST), wind, wind stress, GPH re-analysis data are provided at ~~https://psl.noaa.gov~~https://psl.noaa.gov/ and nutrient data are provided at https://data.marine.copernicus.eu/.

Code availability

The computer codes that support the analysis within this paper are available from the corresponding author on request.

Funding

This work was sponsored by a research grant from the National Research Foundation of Korea (NRF-2021M3I6A1086808), and supported by Research of Long-term Marine Environmental Change in the Yellow Sea and East China Sea Using the Ieodo Ocean Research Station (Ieodo-ORS) form the Korean Hydrographic and Oceanographic Agency (KHOA).

Ethical approval

Not applicable

Declaration of Competing interests

The authors declare no competing interests.

CrediT authorship contribution statement

Dong-Geon Lee: compiled the data, conducted analyses, prepared the figures, and wrote the manuscript. **Jong-Seong Kug:** Designed the research and wrote the majority of the manuscript content. All the authors discussed the study results and reviewed the manuscript.

References

Beardsley, R. C., Limeburner, R., Yu, H., and Cannon, G. A.: Discharge of the Changjiang (Yangtze River) into the East China Sea, Cont. Shelf Res., 4, 57–76, https://doi.org/10.1016/0278-4343(85)90022-6, 1985.

Behrenfeld, M. J., O'Malley, R. T., Siegel, D. A., McClain, C. R., Sarmiento, J. L., Feldman, G. C., Milligan, A. J., Falkowski, P. G., Letelier, R. M., and Boss, E. S.: Climate-driven trends in contemporary ocean productivity, Nature, 444, 752–755, https://doi.org/10.1038/nature05317, 2006.

Carton, J. A., Chepurin, G. A., and Chen, L.: SODA3: A new ocean climate reanalysis, J. Clim., 31, 6967–6983, https://doi.org/10.1175/jcli-d-18-0149.1, 2018.

Cavcar, M.: International Standard Atmosphere, in BS, Anadolu Univ., 30(9), 1–6, 2000.

Chen, C.-T. A.: The Kuroshio intermediate water is the major source of nutrients on the East China Sea continental shelf, Oceanol. Acta, 19, 523–527, 1996.

Chen, C. A.: Buoyancy leads to high productivity of the Changjiang diluted water: a note, Acta Oceanol. Sin., 27, 133–140, 2008.

Chen, C. T. A.: The Three Gorges Dam: Reducing the upwelling and thus productivity in the East China Sea, Geophys. Res. Lett., 27, 381–383, https://doi.org/10.1029/1999GL002373, 2000.

Chen, C. T. A., Ruo, R., Paid, S. C., Liu, C. T., and Wong, G. T. F.: Exchange of water masses between the East China Sea and the Kuroshio off northeastern Taiwan, Cont. Shelf Res., 15, 19–39, https://doi.org/10.1016/0278-4343(93)E0001-O, 1995.

Chen, C. T. A., Liu, C. T., Chuang, W. S., Yang, Y. J., Shiah, F. K., Tang, T. Y., and Chung, S. W.: Enhanced buoyancy and hence upwelling of subsurface Kuroshio waters after a typhoon in the southern East China Sea, J. Mar. Syst., 42, 65–79, https://doi.org/10.1016/S0924-7963(03)00065-4, 2003.

Chen, C. T. A., Yeh, Y. T., Chen, Y. C., and Huang, T. H.: Seasonal and ENSO-related interannual variability of subsurface fronts separating West Philippine Sea waters from South China Sea waters near the Luzon Strait, Deep. Res. Part I Oceanogr. Res. Pap., 103, 13–23, https://doi.org/10.1016/j.dsr.2015.05.002, 2015.

Chowdary, J. S., Hu, K., Srinivas, G., Kosaka, Y., Wang, L., and Rao, K. K.: The Eurasian Jet Streams as Conduits for East Asian Monsoon Variability, Curr. Clim. Chang. Reports, 5, 233–244, https://doi.org/10.1007/s40641-019-00134-x, 2019.

Danielsdottir, M. G., Brett, M. T., and Arhonditsis, G. B.: Phytoplankton food quality control of planktonic food web processes, Hydrobiologia, 589, 29–41, https://doi.org/10.1007/s10750-007-0714-6, 2007.

Dunne, J., Gnanadesikan, A., Sarmiento, J. L., and Slater, R. D.: Technical description of the prototype version (v0) of Tracers Of Phytoplankton with Allometric Zooplankton (TOPAZ) ocean biogeochemical model as used in the Princeton IFMIP* model, Biogeosciences, 7, 3593, 2010.

Dunne, J. P., John, J. G., Shevliakova, E., Stouffer, R. J., Krasting, J. P., Malyshev, S. L., Milly, P. C. D., Sentman, L. T., Adcroft, A. J., Cooke, W., Dunne, K. A., Griffies, S. M., Hallberg, R. W., Harrison, M. J., Levy, H., Wittenberg, A. T., Phillips, P. J., and Zadeh, N.: GFDL's ESM2 Global Coupled Climate–Carbon Earth System Models. Part II: Carbon System Formulation and Baseline Simulation Characteristics*, J. Clim., 26, 2247–2267, https://doi.org/10.1175/JCLI-D-12-00150.1, 2013.

Field, C. B., Behrenfeld, M. J., Randerson, J. T., and Falkowski, P.: Primary production of the biosphere: Integrating terrestrial and oceanic components, Science (80-.)., 281, 237–240, https://doi.org/10.1126/science.281.5374.237, 1998.

Gill, A. E.: Some simple solutions for heat-induced tropical circulation, Q. J. R. Meteorol. Soc., 106, 447–462, https://doi.org/10.1002/qj.49710644905, 1980.

He, X., Bai, Y., Pan, D., Chen, C. T. A., Cheng, Q., Wang, D., and Gong, F.: Satellite views of the seasonal and interannual variability of phytoplankton blooms in the eastern China seas over the past 14 yr (1998-2011), Biogeosciences, 10, 4721–4739, https://doi.org/10.5194/bg-10-4721-2013, 2013.

Henson, S. A., Sarmiento, J. L., Dunne, J. P., Bopp, L., Lima, I., Doney, S. C., John, J., and Beaulieu, C.: Detection of anthropogenic climate change in satellite records of ocean chlorophyll and productivity, Biogeosciences, 7, 621–640, https://doi.org/10.5194/bg-7-621-2010, 2010.

Hill, A. E.: Buoyancy effects in coastal and shelf seas, Sea, 21–62, 1998.

Huang, B., Thorne, P. W., Banzon, V. F., Boyer, T., Chepurin, G., Lawrimore, J. H., Menne, M. J., Smith, T. M., Vose, R. S., and Zhang, H. M.: Extended reconstructed Sea surface temperature, Version 5 (ERSSTv5): Upgrades, validations, and intercomparisons, J. Clim., 30, 8179–8205, https://doi.org/10.1175/JCLI-D-16-0836.1, 2017.

Huang, T. H., Chen, C. T. A., Zhang, W. Z., and Zhuang, X. F.: Varying intensity of Kuroshio intrusion into Southeast Taiwan Strait during ENSO events, Cont. Shelf Res., 103, 79–87, https://doi.org/10.1016/j.csr.2015.04.021, 2015.

Huang, T. H., Chen, C. T. A., Lee, J., Wu, C. R., Wang, Y. L., Bai, Y., He, X., Wang, S. L., Kandasamy, S., Lou, J. Y., Tsuang, B. J., Chen, H. W., Tseng, R. S., and Yang, Y. J.: East China Sea increasingly gains limiting nutrient P from South China Sea, Sci. Rep., 9, 1–10, https://doi.org/10.1038/s41598-019-42020-4, 2019.

Kanamitsu, M., Wesley, E., Jack, W., Yang, S., Hnilo, J. J., Fiorino, M., and Potter, G. L.: NCEP–DOE AMIP-II Reanalysis (R-2), Bull. Am. Meteorol. Soc., 83, 1631–1644, https://doi.org/10.1175/BAMS-83-11-1631, 2002.

Kessler, W. S.: The circulation of the eastern tropical Pacific: A review, Prog. Oceanogr., 69, 181–217, https://doi.org/10.1016/j.pocean.2006.03.009, 2006.

Kim, G. Il, Oh, J. H., Shin, N. Y., An, S. Il, Yeh, S. W., Shin, J., and Kug, J. S.: Deep ocean warming-induced El Niño changes, Nat. Commun., 15, 1–8, https://doi.org/10.1038/s41467-024-50663-9, 2024.

Kim, S. and Kug, J. S.: What Controls ENSO Teleconnection to East Asia? Role of Western North Pacific Precipitation in ENSO Teleconnection to East Asia, J. Geophys. Res. Atmos., 123, 10,406-10,422, https://doi.org/10.1029/2018JD028935, 2018.

Kim, T.-W., Lee*, K., Najja Raymond G, Jeong, H.-D., and Jeong, H. J.: Increasing N Abundance in the Northwestern Pacific Ocean Due to Atmospheric Nitrogen Deposition, Science (80-.)., 334, 505–509, https://doi.org/DOI: 10.1126/science.1206583, 2011.

Kug, J.-S., Jin, F.-F., and An, S.-I.: Two Types of El Niño Events: Cold Tongue El Niño and Warm Pool El Niño, J. Clim., 22, 1499–1515, https://doi.org/10.1175/2008JCLI2624.1, 2009.

Kug, J. S., Choi, J., An, S. Il, Jin, F. F., and wittenberg, A. T.: Warm pool and cold tongue El Niño events as simulated by the GFDL 2.1 coupled GCM, J. Clim., 23, 1226–1239,

668   https://doi.org/10.1175/2009JCLI3293.1, 2010.

669   Kwon, M. H., Jhun, J. G., Wang, B., An, S. Il, and Kug, J. S.: Decadal change in relationship

670   between east Asian and WNP summer monsoons, Geophys. Res. Lett., 32, 1–4,

671   https://doi.org/10.1029/2005GL023026, 2005.

672   ~~Lee, D. G., Oh, J. H., Noh, K. M., Kwon, E. Y., Kim, Y. H., and Kug, J. S.: What controls the~~

673   ~~future phytoplankton change over the Yellow and East China Seas under global warming?,~~

674   ~~Front. Mar. Sci., 10, 1–9, https://doi.org/10.3389/fmars.2023.1010341, 2023.~~

675   Li, T., Wang, B., Wu, B., Zhou, T., Chang, C.-P., and Zhang, R.: Theories on formation of an

676   anomalous anticyclone in western North Pacific during El Niño: A review, J. Meteorol. Res.,

677   31, 987–1006, https://doi.org/10.1007/s13351-017-7147-6, 2017.

678   Li, T., Wang, B., and Chang, C. P.: A review of mechanisms for formation of an anomalous

679   anticyclone in western north pacific during el niño, Multiscale Glob. Monsoon Syst., 31, 91–

680   102, https://doi.org/10.1142/9789811216602_0008, 2021.

681   Liu, K. K., Chao, S. Y., Lee, H. J., Gong, G. C., and Teng, Y. C.: Seasonal variation of

682   primary productivity in the East China Sea: A numerical study based on coupled physical-

683   biogeochemical model, Deep. Res. Part II Top. Stud. Oceanogr., 57, 1762–1782,

684   https://doi.org/10.1016/j.dsr2.2010.04.003, 2010.

685   Liu, S. M., Zhang, J., and Jiang, W. S.: Pore water nutrient regeneration in shallow coastal

686   Bohai Sea, China, J. Oceanogr., 59, 377–385, https://doi.org/10.1023/A:1025576212927,

687   2003.

688   Matsuno, T.: Quasi-Geostrophic Motions in the Equatorial Area, J. Meteorol. Soc. Japan. Ser.

689   II, 44, 25–43, https://doi.org/10.2151/jmsj1965.44.1_25, 1966.

690   Moon, J. Y., Lee, K., Lim, W. A., Lee, E., Dai, M., Choi, Y. H., Han, I. S., Shin, K., Kim, J.

691   M., and Chae, J.: Anthropogenic nitrogen is changing the East China and Yellow seas from

692   being N deficient to being P deficient, Limnol. Oceanogr., 66, 914–924,

693   https://doi.org/10.1002/lno.11651, 2021.

694   Park, T., Jang, C. J., Kwon, M., Na, H., and Kim, K. Y.: An effect of ENSO on summer

695   surface salinity in the Yellow and East China Seas, J. Mar. Syst., 141, 122–127,

696   https://doi.org/10.1016/j.jmarsys.2014.03.017, 2015.

Racault, M. F., Sathyendranath, S., Brewin, R. J. W., Raitsos, D. E., Jackson, T., and Platt, T.: Impact of El Niño variability on oceanic phytoplankton, Front. Mar. Sci., 4, 133, https://doi.org/10.3389/fmars.2017.00133, 2017.

Sathyendranath, S., Brewin, R. J. W., Brockmann, C., Brotas, V., Calton, B., Chuprin, A., Cipollini, P., Couto, A. B., Dingle, J., Doerffer, R., Donlon, C., Dowell, M., Farman, A., Grant, M., Groom, S., Horseman, A., Jackson, T., Krasemann, H., Lavender, S., Martinez-Vicente, V., Mazeran, C., Mélin, F., Moore, T. S., Müller, D., Regner, P., Roy, S., Steele, C. J., Steinmetz, F., Swinton, J., Taberner, M., Thompson, A., Valente, A., Zühlke, M., Brando, V. E., Feng, H., Feldman, G., Franz, B. A., Frouin, R., Gould, R. W., Hooker, S. B., Kahru, M., Kratzer, S., Mitchell, B. G., Muller-Karger, F. E., Sosik, H. M., Voss, K. J., Werdell, J., and Platt, T.: An ocean-colour time series for use in climate studies: The experience of the ocean-colour climate change initiative (OC-CCI), Sensors (Switzerland), 19, https://doi.org/10.3390/s19194285, 2019.

Shi, W. and Wang, M.: Satellite views of the Bohai Sea, Yellow Sea, and East China Sea, Prog. Oceanogr., 104, 30–45, https://doi.org/10.1016/j.pocean.2012.05.001, 2012.

Shin, N. Y., Kug, J. S., Stuecker, M. F., Jin, F. F., Timmermann, A., and Kim, G. Il: More frequent central Pacific El Niño and stronger eastern pacific El Niño in a warmer climate, npj Clim. Atmos. Sci., 5, 1–8, https://doi.org/10.1038/s41612-022-00324-9, 2022.

Son, H. Y., Park, J. Y., Kug, J. S., Yoo, J., and Kim, C. H.: Winter precipitation variability over Korean Peninsula associated with ENSO, Clim. Dyn., 42, 3171–3186, https://doi.org/10.1007/s00382-013-2008-1, 2014.

Tong, Y., Zhao, Y., Zhen, G., Chi, J., Liu, X., Lu, Y., Wang, X., Yao, R., Chen, J., and Zhang, W.: Nutrient Loads Flowing into Coastal Waters from the Main Rivers of China (2006-2012), Sci. Rep., 5, 1–12, https://doi.org/10.1038/srep16678, 2015.

Trenberth, K. E., Large, W. G., and Olson, J. G.: The Mean Annual Cycle in Global Ocean Wind Stress, J. Phys. Oceanogr., 20, 1742–1760, https://doi.org/10.1175/1520-0485(1990)020<1742:TMACIG>2.0.CO;2, 1990.

Wang, B., Wu, R., and Fu, X.: Pacific-East Asian teleconnection: How does ENSO affect East Asian climate?, J. Clim., 13, 1517–1536, https://doi.org/10.1175/1520-0442(2000)013<1517:PEATHD>2.0.CO;2, 2000.

Wang, B., Wang, X., and Zhan, R.: Nutrient conditions in the Yellow Sea and the East China Sea, Estuar. Coast. Shelf Sci., 58, 127–136, https://doi.org/10.1016/S0272-7714(03)00067-2, 2003.

Wang, C. Y., Zheng, X. T., and Xie, S. P.: Enhanced ENSO-Unrelated Summer Variability in the Indo–Western Pacific under Global Warming, J. Clim., 36, 1749–1765, https://doi.org/10.1175/JCLI-D-22-0450.1, 2023.

Wu, Q., Wang, X., He, Y., and Zheng, J.: The Relationship between Chlorophyll Concentration and ENSO Events and Possible Mechanisms off the Changjiang River Estuary, Remote Sens., 15, https://doi.org/10.3390/rs15092384, 2023.

Wyrtki, K. and Meyers, G.: The Trade Wind Field Over the Pacific Ocean, J. Appl. Meteorol., 15, 698–704, https://doi.org/10.1175/1520-0450(1976)015<0698:TTWFOT>2.0.CO;2, 1976.

Xie, S. P., Hu, K., Hafner, J., Tokinaga, H., Du, Y., Huang, G., and Sampe, T.: Indian Ocean capacitor effect on Indo-Western pacific climate during the summer following El Niño, J. Clim., 22, 730–747, https://doi.org/10.1175/2008JCLI2544.1, 2009.

Xie, S. P., Kosaka, Y., Du, Y., Hu, K., Chowdary, J. S., and Huang, G.: Indo-western Pacific ocean capacitor and coherent climate anomalies in post-ENSO summer: A review, Adv. Atmos. Sci., 33, 411–432, https://doi.org/10.1007/s00376-015-5192-6, 2016.

Xu, Y., Wu, Y., Xiu, P., and Ge, J.: Unraveling environmental drivers of chlorophyll seasonal and interannual variability in the East China Sea, 1–20, https://doi.org/10.3389/fmars.2022.951395, 2022.

Yamaguchi, H., Kim, H. C., Son, Y. B., Kim, S. W., Okamura, K., Kiyomoto, Y., and Ishizaka, J.: Seasonal and summer interannual variations of SeaWiFS chlorophyll a in the Yellow Sea and East China Sea, Prog. Oceanogr., 105, 22–29, https://doi.org/10.1016/j.pocean.2012.04.004, 2012.

Yang, K., Cai, W., Huang, G., Hu, K., Ng, B., and Wang, G.: Increased variability of the western Pacific subtropical high under greenhouse warming, Proc. Natl. Acad. Sci. U. S. A., 119, 1–9, https://doi.org/10.1073/pnas.2120335119, 2022.

Yeh, S. W., Kug, J. S., Dewitte, B., Kwon, M. H., Kirtman, B. P., and Jin, F. F.: El Nĩo in a

756 changing climate, Nature, 461, 511–514, https://doi.org/10.1038/nature08316, 2009.

757 Yuan, Y. and Yang, S.: Impacts of different types of El NiñO on the East Asian climate:
758 Focus on ENSO cycles, J. Clim., 25, 7702–7722, https://doi.org/10.1175/JCLI-D-11-00576.1,
759 2012.

760 Zhai, F., Liu, Z., Gu, Y., He, S., Hao, Q., and Li, P.: Satellite-Observed Interannual
761 Variations in Sea Surface Chlorophyll-a Concentration in the Yellow Sea Over the Past Two
762 Decades, J. Geophys. Res. Ocean., 128, 1–23, https://doi.org/10.1029/2022JC019528, 2023.

763 Zhang, J.: Nutrient elements in large Chinese estuaries, Cont. Shelf Res., 16, 1023–1045,
764 https://doi.org/10.1016/0278-4343(95)00055-0, 1996.

765 Zhang, J., Liu, S. M., Ren, J. L., Wu, Y., and Zhang, G. L.: Nutrient gradients from the
766 eutrophic Changjiang (Yangtze River) Estuary to the oligotrophic Kuroshio waters and re-
767 evaluation of budgets for the East China Sea Shelf, Prog. Oceanogr., 74, 449–478,
768 https://doi.org/10.1016/j.pocean.2007.04.019, 2007.

769 Zhang, W., Zhuang, X., Chen, C. A., and Huang, T.: The impact of Kuroshio water on the
770 source water of the southeastern Taiwan Strait: numerical results, Acta Oceanol. Sin., 34, 23–
771 34, https://doi.org/10.1007/s13131-015-0720-x, 2015.

772 Zhang, Y., Yu, Q., Ma, W., and Chen, L.: Atmospheric deposition of inorganic nitrogen to
773 the eastern China seas and its implications to marine biogeochemistry, J. Geophys. Res.
774 Atmos., 115, 1–10, https://doi.org/10.1029/2009JD012814, 2010.

775 Zhao, L. and Guo, X.: Influence of cross-shelf water transport on nutrients and phytoplankton
776 in the East China Sea: A model study, Ocean Sci., 7, 27–43, https://doi.org/10.5194/os-7-27-
777 2011, 2011.

778 .